Mesoscale Subduction at the Antarctic Polar Front Driven by Baroclinic Instability

ALBERTO C. NAVEIRA GARABATO*

Oceanography Laboratories, University of Liverpool, Liverpool, United Kingdom

JOHN T. ALLEN

George Deacon Division, Southampton Oceanography Centre, Southampton, United Kingdom

HARRY LEACH

Oceanography Laboratories, University of Liverpool, Liverpool, United Kingdom

VOLKER H. STRASS

Alfred-Wegener-Institut für Polar und Meeresforschung, Bremerhaven, Germany

RAYMOND T. POLLARD

George Deacon Division, Southampton Oceanography Centre, Southampton, United Kingdom

(Manuscript received 17 April 2000, in final form 25 September 2000)

ABSTRACT

A study of mesoscale subduction at the Antarctic Polar Front (PF) is conducted by use of hydrographic data from a high-resolution, quasi-synoptic survey of the front. The geostrophic velocity and isopycnal potential vorticity (PV) fields are computed, and the ageostrophic flow diagnosed from the semigeostrophic omega equation. It is found that the ageostrophic circulation induced by baroclinic instability counteracts the frontogenesis and frontolysis effected by the confluence and difluence, respectively, of the geostrophic velocity field. Though the sense of the ageostrophic circulation is reversed repeatedly along the front, the existence of PV gradients along isopycnals leads to a net cross-front ''bolus'' transport. In response to a reversal of this gradient with depth (a necessary condition for the onset of baroclinic instability), the bolus transport is northward at the protruding temperature minimum layer that characterizes the PF, and southward above. This net cross-front overturning circulation acts to flatten the isopycnals of the front and results in a subduction of the temperature minimum layer as it progresses northward along isopycnals. Consistently, a net baroclinic conversion rate of approximately 1 $cm^2\ s^{-2}\ d^{-1}$, corresponding to a net subduction rate of $O(20\ m\ yr^{-1})$, is calculated in the survey area. The similarity between the PV field of the PF and other Southern Ocean fronts suggests that the authors' results may also be applicable there. This has profound implications for the understanding of the zonation of the Antarctic Circumpolar Current.

1. Introduction

The Southern Ocean is a major region of formation of deep and intermediate water masses, and plays a vital role in the global interchange of basin water through the eastward flow of the Antarctic Circumpolar Current (ACC). Due precisely to its circumpolar character, the dynamical nature of the ACC is distinct from that of wind-driven gyre circulations in zonally bound basins, many features of which have been successfully explained by a variety of theories based on Sverdrup dynamics (e.g., Dewar and Marshall 1994; Sakamoto 1999). Though the ACC is also believed to be basically wind-driven (Nowlin and Klinck 1986; Ivchenko et al. 1996) a range of aspects concerning its dynamics remains poorly understood. Among these is the structuring of the flow into a series of narrow jets associated with deep-reaching, circumpolar density fronts (Orsi et al. 1995; Belkin and Gordon 1996) that crucially constrain the pathways and distributions of water masses (e.g., Peterson and Whitworth 1989). Evidence exists linking the locations of particular frontal bands to meridional

* Current affiliation: School of Environmental Sciences, University of East Anglia, Norwich, United Kingdom.

Corresponding author address: Alberto C. Naveira Garabato, School of Environmental Sciences, University of East Anglia, Norwich NR4 7TJ, United Kingdom.
E-mail: a.naveira-garabato@uea.ac.uk

gradients in the properties of the Ekman and net surface buoyancy fluxes (Deacon 1982; Kazmin and Rienecker 1996) as well as to topographic steering (Hughes and Killworth 1995; Gille 1997). However, the most significant insight into the banded nature of the ACC has been provided by a number of numerical experiments (Vallis and Maltrud 1993; Treguier and Panetta 1994; Marshall and Adcock 1998; Sinha and Richards 1999) performed in the conceptual framework of the theory of geostrophic turbulence.

The theory of geostrophic turbulence (Rhines 1975, 1979) studies the unforced, nonlinear motion of fluids that are near to a state of geostrophic and hydrostatic balance. A fundamental result of the theory predicts that the free evolution of an initial field of turbulent eddies will involve a cascade of energy to small wavenumbers and a simultaneous cascade of potential enstrophy (potential vorticity variance) to large wavenumbers. In physical space, this translates into the formation of larger eddies with their vorticity sheared out into ever finer filaments. Further, when an analogous scenario is considered on a β plane, a mean-state potential vorticity (PV) field is provided by the spherical shape of the earth, and the stretching of PV surfaces (on which the potential enstrophy cascade relies) is constrained in a certain manner by planetary curvature. It has been shown (Rhines 1979) that this constraint may be expressed as an upper bound to the migration of dominant eddies toward large scales [the Rhines scale, defined as $(U\beta^{-1})^{1/2}$, where U is a characteristic horizontal speed of the flow and β the meridional gradient of the Coriolis parameter] and that the anisotropy introduced by the β effect will cause the eddies to flatten and thereby concentrate energy on the zonal direction. The end state of the cascade will then tend to be dominated by a series of bands of eastward and westward flow alternating with a length scale of the order of the Rhines scale. This scenario is clearly reminiscent of the observed structuring of the ACC into eastward frontal jets with little flow in between.

Despite recent indications that the Rhines scale may adequately describe flow structure in numerical models of the Southern Ocean (Sinha and Richards 1999), direct observational support for the applicability of the above ideas to the ACC system is still scarce. The choice of U and β in the calculation of the Rhines scale is, to some extent, ambiguous, whereas various assumptions of the theory of geostrophic turbulence (in particular, that of unforced flow) do not strictly apply to the ACC. It can only be speculated that the research of C. W. Hughes and coworkers (Hughes et al. 1998, and references therein) on the ability of the ACC to act as a Rossby waveguide might indicate that the postulates of the theory of geostrophic turbulence can contribute to a valid description of ACC dynamics. Indeed, it may be reasoned that when the diameter of the dominant eddies approaches the Rhines scale the mean-state PV field induced by planetary curvature starts providing a significant restoring force for transient motions crossing PV contours, and a Rossby wave is set up. Therefore, the detection of intense Rossby wave activity within the ACC could well be symptomatic of the presence of a geostrophic turbulent eddy field in the process of shaping the banded anatomy of the current system.

The eddy activity of the Southern Ocean has been mapped in various altimetric and numerical studies (Chelton et al. 1990; Shum et al. 1990; Morrow et al. 1992; Stevens and Killworth 1992; Wilkin and Morrow 1994; Gille 1997). Eddy kinetic energy (EKE) levels are high in relation to most open ocean regions of the globe. Surface EKE maxima generally appear in association with certain topographic obstructions and along a band centered around the axis of the ACC. Whereas the former are believed to be due to the action of topographic lee waves, the latter are most likely connected to mesoscale variability in the vicinity of the Antarctic Polar Front (PF). As if to reinstate the existence of an intimate link between eddy activity and fronts, reports also exist of frequent frontal meandering and shedding of eddies in other frontal regions of the ACC, such as the Subtropical Frontal Zone (Lutjeharms and Valentine 1988; Holliday and Read 1998) and the Subantarctic Front (Park and Gambéroni 1997; Rintoul et al. 1997) in the northern ACC. The importance of mesoscale eddies in the buoyancy and momentum balances of the Southern Ocean has been emphasized by a number of numerical experiments (Johnson and Bryden 1989; Treguier and McWilliams 1990; Ivchenko et al. 1997; Stevens and Ivchenko 1997; Best et al. 1999).

The nature of the eddies' role in such large-scale balances has been investigated in detail within several modeling studies of mesoscale activity in a frontal zone (see. e.g., Spall 1995, and references therein). According to these, eddy fluxes of buoyancy and momentum are different expressions of a downward transfer of water (subduction) occurring at the front. As the dynamical properties of the deep ocean are largely set when water parcels were last in contact with the atmosphere, the process of subduction is thought to be of paramount importance for the large-scale circulation and stratification of the ocean. Though subduction driven by large-scale Ekman convergence has been long regarded as dominant, scaling estimates by Follows and Marshall (1994) suggest that mesoscale subduction at frontal regions may be comparable in magnitude.

In this paper, we present evidence of mesoscale subduction in the PF region south of Africa and discuss the dynamics of the process. The implications of our findings for the maintenance of the frontal structure of the ACC are explored and their consistency with the predictions of the theory of geostrophic turbulence examined briefly.

We make use of hydrographic data from two nested mesoscale surveys of a segment of the PF near 10°E. Their combined quasisynopticity and high spatial resolution are ideally suited for the analysis of mesoscale processes and make the dataset superior to satellite or

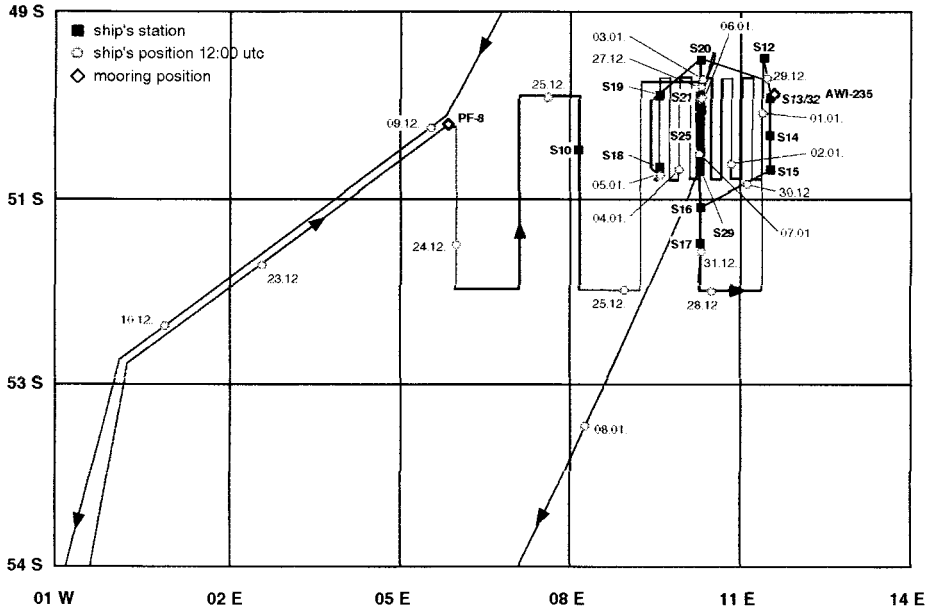

FIG. 1. Cruise track of PFS *Polarstern* Expedition ANT XIII/2 (4 Dec 1995–24 Jan 1996) in the main working area.

conventional CTD station data. The dataset is presented in section 2. In section 3, the hydrographic background encountered in the surveyed region is described. Based on the measured density and velocity fields, the three-dimensional flow in the surveyed area is diagnosed in section 4. This is achieved by separately inferring the geostrophic and ageostrophic components of the flow, placing emphasis on the problem of computing the latter. In section 5, we give a dynamical explanation of the diagnosed flow patterns and examine the cross-frontal buoyancy fluxes implied by the flow. Finally, in section 6 we summarize our findings and discuss their relevance for the understanding of the zonation of the ACC.

2. The ANT XIII/2 dataset

The dataset was collected during cruise ANT XIII/2 of the German polar research vessel PFS *Polarstern* between 4 December 1995 and 24 January 1996. It encompassed a long transect (5–11 December 1995) southward from Cape Town toward Kapp Norvegia (Antarctica) to locate the positions of the ACC fronts, a coarse scale survey (CSS, 24–29 December 1995) to map a large-scale meander of the PF, and a finescale survey (FSS, 1–5 January 1996) across a region of high horizontal hydrographic gradients in the northeastern quadrant of the CSS area (Fig. 1). The CSS consisted of six parallel meridional sections 75 km apart and covered an area of approximately 375 km zonally $\times$ 220 km meridionally. The FSS involved 11 meridional legs 13 km apart and spanned an area of 130 km $\times$ 130 km. Because of the enhanced horizontal resolution of the FSS, subsequent analysis will concentrate on the FSS region.

Using an undulating profiler (SeaSoar) equipped with a Neil Brown Mark III CTD the hydrography of the upper water column was sampled, while an RD Instruments 150-kHz vessel-mounted acoustic Doppler current profiler (VM-ADCP) was employed to measure currents. The depth range of SeaSoar was ~400 m, with an 8-m vertical resolution after filtering and interpolation. The VM-ADCP data was averaged every 2 min while under way (implying a horizontal resolution of 0.5 km) and reached slightly deeper than 300 m, with a vertical resolution of 4 m.

Complementing the SeaSoar/VM-ADCP monitoring of the upper ocean, the deeper physical structure of the PF region was investigated by means of an array of sparse full-depth hydrographic stations at which a Neil Brown Mark III CTD was cast in conjunction with a General Oceanics Rosette Bottle Sampler. In addition, a mooring (AWI-235) was deployed at the northeastern corner of the FSS area including an RDI 150-kHz NB self-contained ADCP and six Aanderaa RCM-8 rotor current meters distributed in such a fashion as to profile the full depth of the water column.

3. Hydrography of the PF region

The hydrographic situation in the surveyed sector of the PF is best shown by a potential temperature–salinity (θ–S) diagram (Fig. 2), where four major water masses can be seen. Antarctic Surface Water (AASW) occupies the upper ocean above 100 m. Relatively warm and fresh, it acquires its properties from solar warming and ice melt in the heating season. Immediately below, in the depth range 150–250 m, the ''Winter Water'' (WW) is a remnant of a deep winter mixed layer resulting from

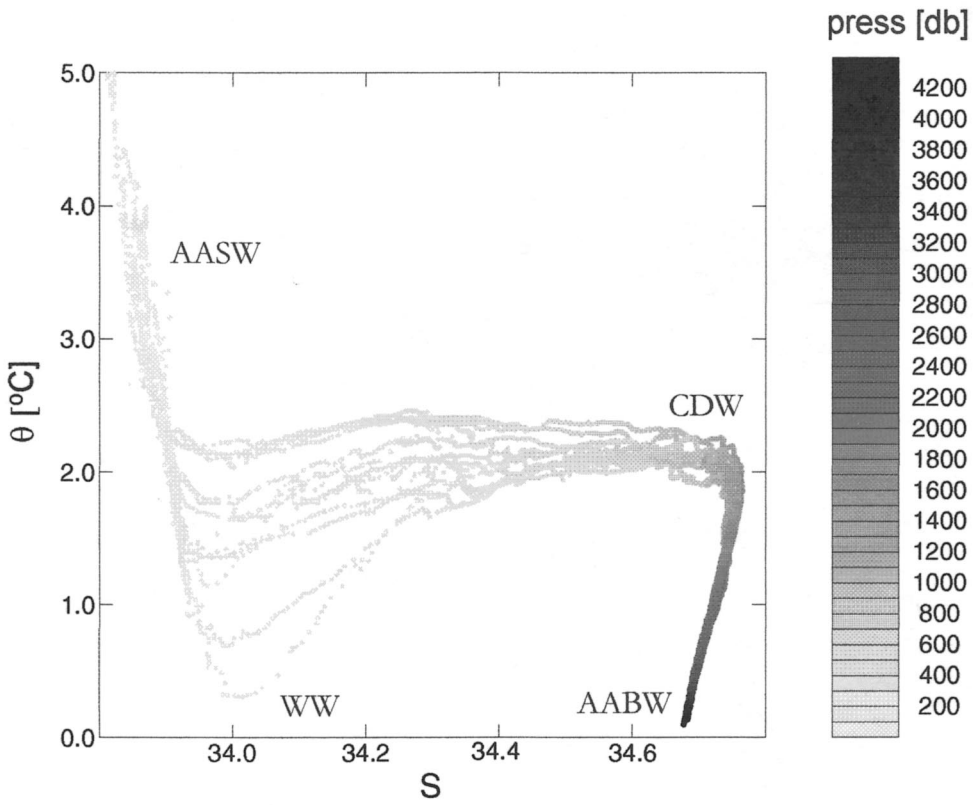

FIG. 2. θ–S diagram for the CTD transect along 10.3°E. The pressure at which measurements were conducted is displayed in the shading of dots. The water masses present in the region are identified by the acronyms AASW (Antarctic Surface Water), WW (Winter Water). CDW (Circumpolar Deep Water), and AABW (Antarctic Bottom Water).

vertical convective processes induced by cooling and sea ice formation during austral winter (Mosby 1934; Whitworth and Nowlin 1987). Circumpolar Deep Water (CDW) derives its characteristics from North Atlantic Deep Water intruding into the Southern Ocean in the southwest Atlantic (Whitworth and Nowlin 1987), is relatively warm and saline, and spans most of the water column below 300 m. Only near the ocean floor is there the colder, fresher Antarctic Bottom Water.

This arrangement of water masses has a double pycnocline structure associated with it, with stratification reaching peak values in the region of transition from AASW to WW (the summer pycnocline) and at the base of the WW (the winter pycnocline). Historically, the temperature of the WW has been employed to trace the position of the PF at many sites around Antarctica. Following Botnikov (1963) and a number of other authors, Belkin and Gordon (1996) conclude that a most reliable indicator of the PF is the northern limit of the 2°C contour at the temperature minimum of WW.

Figure 3a displays a contour map of temperature (T) at the temperature minimum (T-min) in the CSS area, with the currents at 184 m measured by the VM-ADCP shown by vectors. A vigorous jet, linked to the PF, may be seen flowing east along ~50.2°S, aligned with the 1.8°C temperature contour. A second jet is observed to the south, meandering with ~250 km wavelength between 51° and 52.5°S and following the 1.0°C contour closely. This jet lies south of the conventionally defined PF and (as revealed by inspection of the deep CTD data along 10.3°E) north of the Southern ACC Front, the northernmost of the circumpolar frontal bands south of the PF (Orsi et al. 1995). It would thus appear that the jet and the associated temperature gradient are expressions of a rather localized frontal branching, probably resulting from local bathymetry. We suspect that this frontal feature bears a relation to the PF, which has been previously reported to split in the region south of Africa (e.g., Lutjeharms and Valentine 1984; Holliday and Read 1998), and have thus followed Strass et al. (2000) in naming it Southerly Polar Front (SPF).

The PF and SPF appear to diverge near ~6°E and tend to converge near ~10°E. An anticyclonic (anticlockwise) recirculation is observed at 51.5°S, 8.5°E between the two frontal bands and coupled to the southern one. There is also a weak cyclonic (clockwise) feature near 50.8°S, 9.0°E that may form a dipole pair with the anticyclone to the south. A second, more vigorous cyclonic recirculation occurs at 50.5°S, 11.2°E (C_1) and appears to touch the PF. Having performed a more detailed description of the CSS observations, Strass et al. showed that the hydrographic and circulation patterns

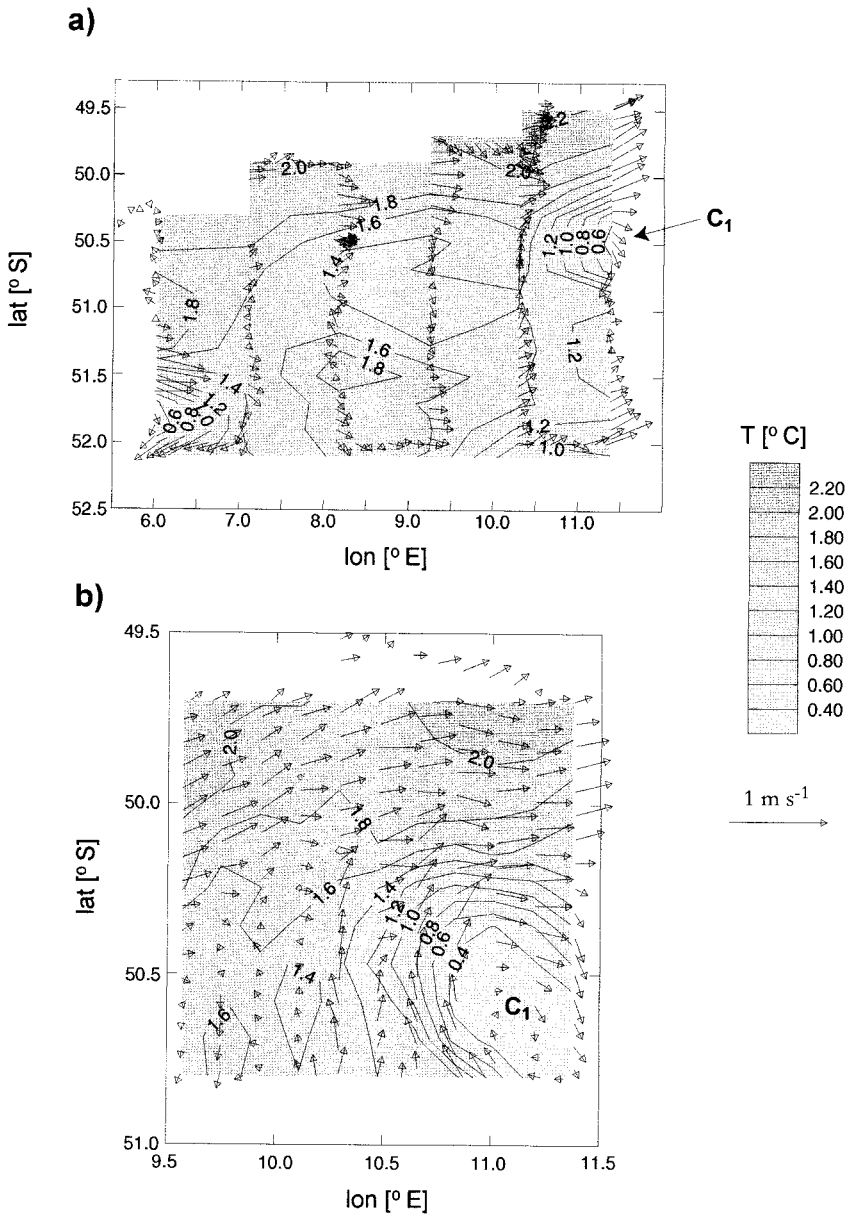

FIG. 3. Horizontal distribution of temperature at the temperature minimum (~180 m depth) and VM-ADCP current vectors at 184 m in (a) the CSS area and (b) for the FSS area. C_1 denotes the cyclonic feature mentioned in the text.

outlined above are not exclusive of the *T*-min layer, but hold for the entire depth range of SeaSoar.

Despite the mean period of 8 days elapsed between the two surveys, the hydrographic fields observed in the FSS were highly similar to those sampled in the area during the CSS, albeit with improved resolution. Figure 3b shows *T* at the *T*-min and VM-ADCP currents as measured during the FSS. A quasi-zonal, smoothly meandering eastward jet (corresponding to the PF) is visible near 50°S and the cyclonic recirculation C_1 appears now to be closed and centered at 50.6°S, 11.1°E. The pronounced *T*-min at the core of this eddy indicates its being shed from the SPF to the south. In the southwestern corner of the FSS area is a weak cyclonic meander that appears to couple with the eddy C_1, thus forming a full wave pattern.

4. Diagnosis of the geostrophic and ageostrophic flow in the FSS

a. Diagnosis of the geostrophic flow

Diagnosis of the geostrophic flow in the FSS was hindered by the existence of tidal and inertial oscillations, described by Strass et al. from the AWI-235 mooring. Inertial oscillations of amplitude ~0.2 m s^{-1} and

period 15.6 h were ubiquitous within the mixed layer, though barely detectable below it. The tidal signal (of amplitude $\sim$0.08 m s^{-1}) was more barotropic and of semidiurnal period. This inertial and tidal motion was not detectable in the VM-ADCP currents, for it was eclipsed by the periodic signal ($\sim$0.4 m s^{-1} amplitude, 17 h period) resulting from the repeated crossing of the PF jet.

A procedure was designed to filter out high-frequency motions from the VM-ADCP record that relied on the assumption of horizontal coherency of inertial and tidal oscillations over the FSS area. This seemed justified by the fact that the length scale of the weather systems that set up inertial oscillations is an order of magnitude larger than the lateral extent of the survey, that the presence of an amphidromic point is not predicted in the area by tidal models (Kantha 1995), and that the depth of the surface mixed layer was approximately uniform throughout the surveyed region. The signal from the current meter array AWI-235 was detrended, then merged in a common time and depth base with the VM-ADCP current record and subtracted from the latter. Linear interpolation was used at the depth levels where no current meters had been deployed, as the depth range of high inertial vertical shear (the mixed layer base) was well resolved by the moored current meters. The vertical shear of VM-ADCP currents at the bottom of the mixed layer was noticeably reduced after the subtraction and, overall, horizontal velocity vectors tended to align with potential density contours. The root-mean-square (rms) deviation between the raw and corrected VM-ADCP velocity field was 0.07 and 0.08 m s^{-1} for zonal and meridional velocity respectively.

To calculate the geostrophic flow and other dynamic variables SeaSoar potential density and filtered VM-ADCP velocity need to be interpolated onto a regular grid. This was done by first averaging the data vertically into 8-m bins and then gridding horizontally along each depth onto a fine mesh of 50 $\times$ 50 points. The anisotropic Gaussian interpolation routine described by Allen and Smeed (1996) was used for the horizontal gridding. Characteristic horizontal *e*-folding length scales of d_x = 25 km and d_y = 12 km were applied, respectively, in the zonal and meridional directions. The choice of these length scales was based on the anisotropic autocorrelation properties of the potential density field.

For computing the geostrophic circulation in the FSS the velocity field was constrained to be nondivergent and in thermal wind balance with the density field, which is measured with far better accuracy. The thermal wind equations state that

$$\frac{\partial u_g}{\partial z} = \frac{g}{f\rho_0}\frac{\partial \rho}{\partial y} \tag{1}$$

and

$$\frac{\partial v_g}{\partial z} = -\frac{g}{f\rho_0}\frac{\partial \rho}{\partial x}, \tag{2}$$

where u_g and v_g are the eastward and northward components of the geostrophic velocity vector $\mathbf{u}_g$ relative to a Cartesian frame of reference (x, y, z) rotating with the earth, g is the acceleration due to gravity, $f = 2\Omega \sin \phi$ is the Coriolis parameter (with ϕ representing latitude and Ω as the angular velocity of the earth's rotation), ρ denotes potential density, and ρ_0 is a reference potential density. As carefully pointed out by Rudnick (1996), Eqs. (1)–(2) should, strictly speaking, refer to in situ density rather than potential density. Errors introduced by using potential density are nevertheless small because the maximum depth of the SeaSoar/VM-ADCP measurements did not exceed 400 m.

The algorithm in Rudnick (1996) was employed to incorporate density and velocity data from the entire VM-ADCP vertical range in the calculation of the geostrophic flow at a certain reference depth, from which the geostrophic velocity field at other depths was obtained through Eqs. (1)–(2). The resulting geostrophic velocity field was essentially barotropic and insensitive to the choice of reference level. Furthermore, it remained very similar to the filtered VM-ADCP velocities, with an rms deviation of 0.03 m s^{-1} for either component of the flow and correlation coefficients of 0.97 (u) and 0.92 (v) between both fields. The diagnosed geostrophic circulation will be presented in section 5.

b. Diagnosis of the ageostrophic flow

Ageostrophic motions are difficult to measure directly. By definition, their zonal and meridional components (u_a and v_a, respectively) are of magnitude $u_a \sim \mathrm{R_o} u_g$ and $v_a \sim \mathrm{R_o} v_g$, where $\mathrm{R_o} = U f^{-1} L^{-1}$ is the Rossby number of the local flow and L is a characteristic horizontal length scale of the flow. In the ocean $\mathrm{R_o}$ is typically less than 1, and the geostrophic velocity dominates the mesoscale circulation. Similarly, the vertical component of the ageostrophic flow (w) can be predicted, through a scale analysis of the momentum equations, to be 10^{-5}–10^{-3} m s^{-1}. This figure borders the instrumental uncertainty of state-of-the-art current meters and is far smaller than vertical flows associated with surface waves (up to 1 m s^{-1}) and internal waves and tides (10^{-3}–10^{-1} m s^{-1}).

The ageostrophic velocity field, however, can also be inferred from synoptic density and geostrophic velocity fields by applying a set of dynamical constraints. This set of constraints is most elegantly expressed in a diagnostic relationship for w known as the omega equation (Hoskins et al. 1978; Leach 1987; Tintoré et al. 1991; Pollard and Regier 1992; Rudnick 1996; Allen and Smeed 1996; Viúdez et al. 1996c), from which u_a and v_a can be derived using continuity. The high accuracy of the omega equation has been demonstrated in the context of numerical models of meandering fronts (Strass 1994; Pinot et al. 1996; Viúdez et al. 1996a). Here, we use a version of the equation based on the semigeostrophic (SG) dynamical balance.

The SG omega equation (Hoskins and Draghici 1977) is the least restrictive approximation to the generalized omega equation, which is primitive equation based and hence not strictly diagnostic (Viúdez et al. 1996b). Unlike the more widely employed quasigeostrophic version, semigeostrophy does not require that R_o be small and so provides an improved description of high R_o scenarios (Pinot et al. 1996), such as those involving sharp fronts. The disadvantage of the SG omega equation is that it must be transformed to a different coordinate system (the geostrophic space, defined below) if it is to be expressed solely in terms of easily measured variables like ρ and $\mathbf{u}_g$. The transformation to geostrophic space forces the equation to an f plane, though past experience (Fiekas et al. 1994) shows that the error introduced by this is small (see appendix).

Hoskins (1975) and Hoskins and Draghici (1977) provide a lengthy discussion on the properties of the SG omega equation and the approximations involved in its derivation. Following the latter, the geostrophic space may be defined by $X = x + f^{-1}v_g$, $Y = y - f^{-1}u_g$, $Z = z$, $T = t$. If a new ageostrophic velocity vector (u_a^*, v_a^*, w^*) is introduced such that $u_a^* = u_a + f^{-1}w(\partial v_g/\partial Z)$, $v_a^* = v_a - f^{-1}w(\partial u_g/\partial Z)$, and $w^* = J^{-1}w$, where $J = 1 + f^{-1}\zeta_g$ is the Jacobian of the transformation to geostrophic space and $\zeta_g = \partial v_g/\partial x - \partial u_g/\partial y$ the vertical component of the geostrophic relative vorticity, the SG omega equation can be written as

$$\nabla_H^2(q_g w^*) + f^2\frac{\partial^2 w^*}{\partial Z^2} = 2\nabla_H \cdot \mathbf{Q}_g.$$

Here $q_g = -\rho_0^{-1}gJ(\partial\rho/\partial Z)$ is the geostrophic PV, and the geostrophic Q-vector is described by

$$\mathbf{Q}_g \equiv (Q_{gX}, Q_{gY}) = \frac{g}{\rho_0}\left(\frac{\partial \mathbf{u}_g}{\partial X}\cdot\nabla_H\rho, \frac{\partial \mathbf{u}_g}{\partial Y}\cdot\nabla_H\rho\right),$$

with ($\nabla_H \equiv \partial/\partial X, \partial/\partial Y$).

A simultaneous overrelaxation solver with Chebyshev acceleration was employed to fully invert the SG omega equation. This solver was tested against one based on Stone's strongly implicit procedure with no significant discrepancies in the results being detected. After Allen and Smeed (1996), we minimized errors near boundaries by exclusively using centered differences in calculating spatial gradients. This was at the expense of losing information along the rim of the surveyed region.

Solving elliptic equations requires specification of boundary conditions on the enclosing surface of the domain. In the present case, Dirichlet conditions ($w = 0$) at the ocean surface were well within the error of the solution. On the lateral boundaries, Neumann conditions ($\partial w/\partial \mathbf{n} = 0$, where $\mathbf{n}$ is a unit vector perpendicular to the boundary) were imposed. This is equivalent to disregarding the contribution of the vertical flow to the local vorticity balance. In a quasigeostrophic sense, this contribution is small compared with the conversion of horizontal to vertical vorticity by the geostrophic vertical shear (Pollard and Regier 1992). As the geostrophic gradient Froude numbers (which quantify this conversion, see section 5 for definition) were small in the FSS (Naveira Garabato et al. 2000) the use of lateral Neumann conditions is likely to be approximately valid throughout.

In contrast, the choice of adequate bottom boundary conditions proved to be critical. Ideally, Dirichlet conditions at the seafloor would be used, but in practice this is only possible in shallow areas. In the FSS only the top ~400 m of a ~3500 m deep ocean were sampled with enough horizontal resolution. Setting either w or its vertical gradient to zero at the deepest surveyed level, as has been done in the past in other regions of the ocean (e.g., Pollard and Regier 1992; Allen and Smeed 1996) was arbitrary and unrealistic. Applying Dirichlet bottom boundary conditions assumes that the dominant baroclinic mode of vertical velocity has a zero-crossing point at the deepest level of the SeaSoar survey. On the other hand, Neumann conditions would force the vortex stretching term ($\partial w/\partial z$) to vanish near the bottom of the surveyed volume or, equivalently, presuming the existence of local extrema of vertical velocities at this depth. Both extreme cases are highly unlikely and result in totally different vertical structures for w. Though the geographical positions and sign of vertical velocity patches were unaffected by the choice of bottom boundary conditions, peak magnitudes were changed by an order 1 factor.

We used temporally averaged velocity profiles from mooring AWI-235 (Fig. 4) to optimize our choice. The PF jet dominated the mean zonal flow. This was eastward and equivalent barotropic, reaching 0.25 m s^{-1} in the mixed layer and decaying with depth to 0.09 m s^{-1} at 1100 m. In contrast, the mean meridional velocity was an order of magnitude smaller and reversed with depth near 150 m. Below this level, northward flow peaked at ~600 m, where Strass et al. noted a reversal in the rotation of the mean velocity vector with depth following the β spiral, a dynamical process characteristic of the large scale. It was also at this depth that the deepest updomed isopycnal associated with the eddy C_1 was detected in the CTD transect along 10.3°E. As the influence of the mesoscale dynamics ceased near 600 m and the measured peak northward flow at that depth implies, through continuity, vanishing vertical velocities, we decided to apply Dirichlet bottom boundary conditions at 600 m.

The gridded SeaSoar data, however, reached only to 349 m. In order to extend the dataset to 600 m, the deep potential density field was approximated by second-order polynomial surfaces fitted to sparse data from the 11 deep CTD casts conducted in the survey area (Fig. 1). The gridded SeaSoar and extrapolated potential density fields were blended together by means of a weighting function with an e-folding vertical length scale of 50 m (derived from inspection of the SeaSoar data).

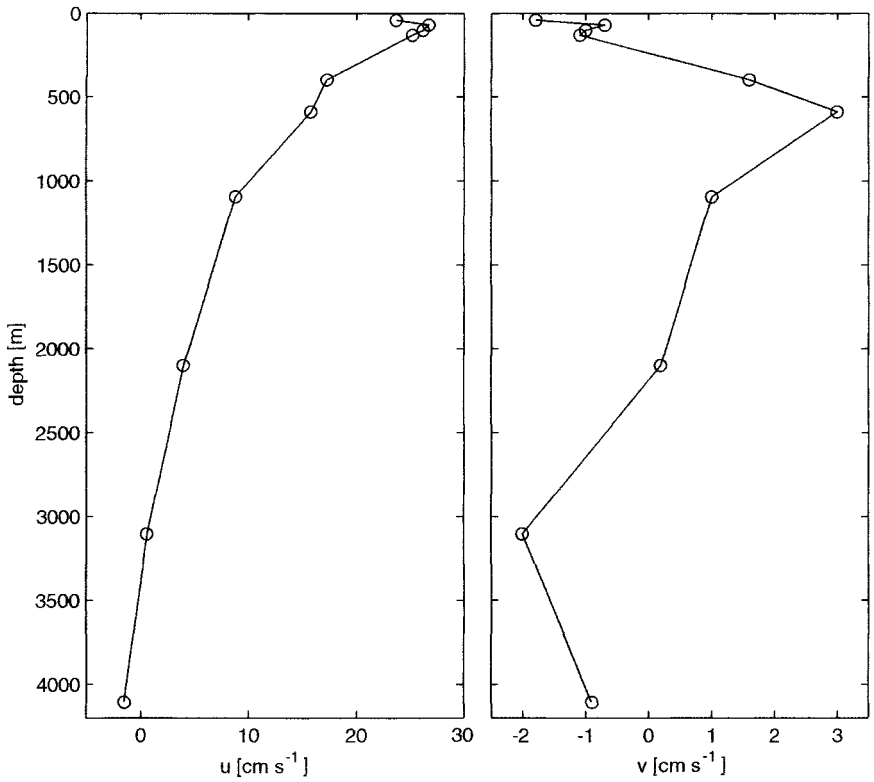

FIG. 4. Vertical profiles of the eastward and northward components of the mean (from 29 Dec 1995–20 Jan 1996) flow measured by mooring AWI-235.

This avoided the appearance of sudden vertical gradients in the forcing term of the omega equation, arising from the dissimilarity in the horizontal resolution of the observed and the extrapolated fields. Though only broadly accurate, the extrapolated field reflected well all major hydrographic features, like the frontal isopycnic slope and the depths of stratification maxima, and the horizontal variation of the potential density field.

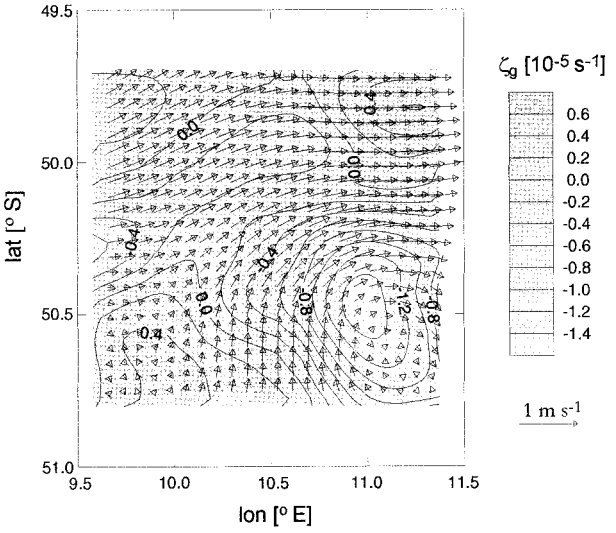

FIG. 5. Horizontal distribution of geostrophic relative vorticity ζ_g (contours) and geostrophic velocity (vectors) at 277 m in the FSS area. The characteristic uncertainties in the magnitudes of u_g, v_g, and ζ_g are estimated as 5%, 5%, and 10%, respectively.

5. Results

The geostrophic flow calculated in section 4a (Fig. 5) supports the inferences about the circulation in the FSS region drawn in section 3. A strong geostrophic jet, associated with the PF, meanders along the pronounced T gradient crossing the northern part of the FSS area in an east-northeast direction (Fig. 3a). The PF jet is flanked by a band of cyclonic relative vorticity (of $0.6 \times 10^{-5}\,\mathrm{s}^{-1}$ or $-0.05f$) encompassing the leading edge of the meander ridge and an anticyclonic region at the northeast of the survey area ($0.6 \times 10^{-5}\,\mathrm{s}^{-1}$ or $-0.05f$), where the trough of the jet lies. Another core of strong geostrophic flow is observed along the rim of the eddy C_1 running parallel to WW isotherms. Here the largest negative values of ζ_g ($-1.5 \times 10^{-5}\,\mathrm{s}^{-1}$ or $0.13f$) in the FSS are found. The meander in the southwest, in the trough of the wavelike folding described in section 3, is weakly anticyclonic ($0.5 \times 10^{-5}\,\mathrm{s}^{-1}$ or $-0.04f$).

The vertical velocity field at 189 m is displayed in Fig. 6. At other depths the horizontal pattern is similar,

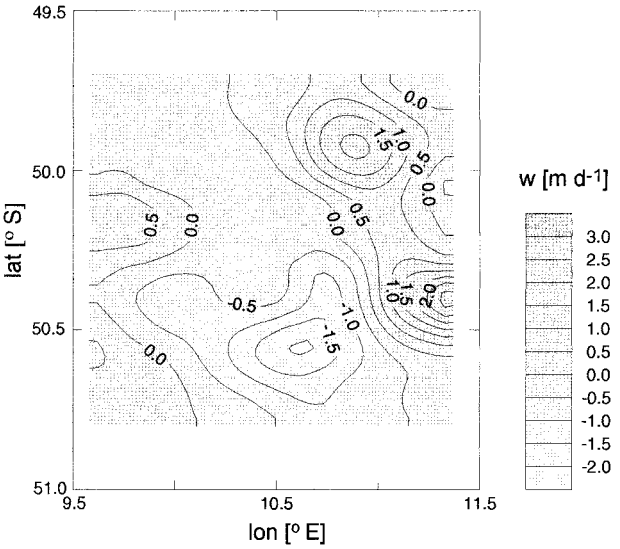

FIG. 6. Horizontal distribution of vertical velocity w at 189 m as diagnosed from the SG omega equation. The characteristic uncertainty in the magnitude of w is estimated as 50%.

with the magnitude of the flow varying like the first baroclinic mode with zero flow at the surface and 600 m, and peak values near 280 m. An area of downwelling (upwelling) can be observed on the upstream (downstream) flank of the cyclonic eddy C_1, in good agreement with the predictions of baroclinic wave theory (e.g., Holton 1978; Gill 1982). The slight meandering of the PF jet to the north causes a similar pattern of vertical motion, with downwelling (upwelling) on the leading (trailing) edge of crests.

The corresponding field of horizontal ageostrophic velocity, inferred from continuity, is shown in Fig. 7. Near the surface (Fig. 7a) the horizontal ageostrophic flow is anticyclonic along the flank of the eddy C_1 and reaches 0.4 cm s^{-1}. A broader band of weaker ($\sim$0.2 cm s^{-1}) southwestward flow occurs northwest of the eddy and turns southward after convergence with the weakly cyclonic, eastward flow ($\sim$0.1 cm s^{-1}) at the southwestern end of the FSS area. Though the structure of the horizontal ageostrophic circulation is complicated by the interaction of the PF jet, the eddy C_1, and the meander to the southwest, the horizontal ageostrophic velocity vectors are directed from upwelling to downwelling patches. This pattern is reversed below the depth of maximum vertical flow (Fig. 7b).

In order to relate the behavior of the ageostrophic flow to that of the geostrophic circulation, we calculate the frontogenesis function (Hoskins 1982) in the quasigeostrophic limit:

$$F_{\mathrm{Ho}} = \left(\frac{g}{\rho_0}\right)^2 \frac{D_{qg}|\nabla_h \rho|^2}{Dt} = 2\frac{g}{\rho_0}\nabla_h \rho \cdot [N^2 \nabla_h w - \mathbf{Q}_{qg}],$$

where $\nabla_h \equiv (\partial/\partial x, \partial/\partial y)$, $D_{qg}/Dt \equiv \partial/\partial t + u_g \partial/\partial x + v_g \partial/\partial y + w\partial/\partial z$ is the Lagrangian time derivative following the geostrophic and vertical flow, the Brunt–Väisälä frequency is defined as

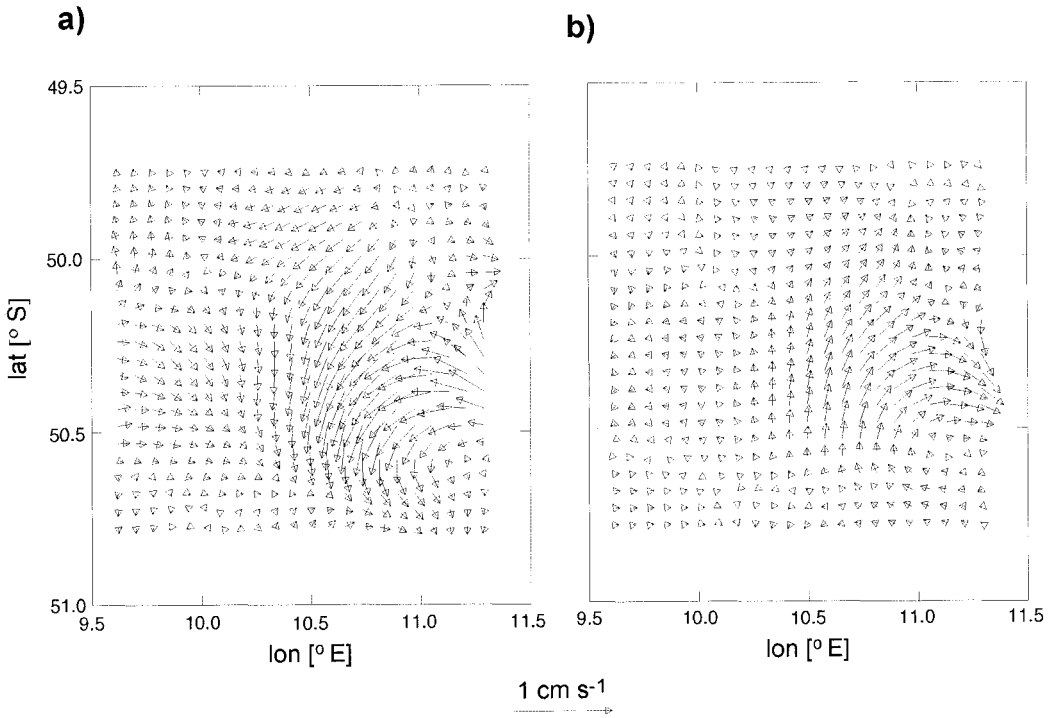

FIG. 7. Horizontal ageostrophic current vectors in the FSS area at (a) 13 m and (b) 333 m. The characteristic uncertainty in the size of each of the horizontal components of the ageostrophic velocity vector is estimated as 35%.

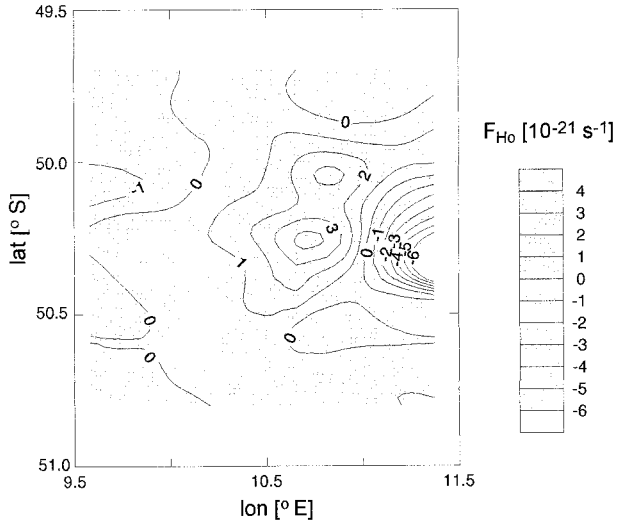

FIG. 8. Horizontal distribution of the Hoskins frontogenesis function F_{Ho} at 277 m in the FSS area. The characteristic uncertainty in the magnitude of F_{Ho} is estimated as 60%.

$$N^2 = -\frac{g}{\rho_0}\frac{\partial \rho}{\partial z}, \quad \text{and} \quad \mathbf{Q}_{qg} = \frac{g}{\rho_0}\left(\frac{\partial \mathbf{u}_g}{\partial x}\cdot\nabla_h\rho, \frac{\partial \mathbf{u}_g}{\partial y}\cdot\nabla_h\rho\right)$$

is the quasigeostrophic Q vector; F_{Ho} is proportional to the rate of change of the squared horizontal gradient of potential density following the flow and can thus detect regions of confluence or difluence in the geostrophic velocity field. In the FSS area, the strongest frontogenesis (F_{Ho} values in excess of 2×10^{-21} s^{-5}) occurs at the confluence of the western flank of the eddy C_1 with the PF jet (Fig. 8), whereas frontolysis ($F_{\mathrm{Ho}} < -6 \times 10^{-21}$ s^{-5}) dominated in the difluent region near the eastern rim of the eddy.

Comparing Figs. 5 and 8, it is observed that in a region of frontogenesis (positive F_{Ho}), water parcels are geostrophically accelerated downstream, whereas in a frontolytic area (negative F_{Ho}) the geostrophic flow decelerates downstream. The SG horizontal momentum equations after subtraction of the geostrophic balance

$$\frac{Du_g}{Dt} = fv_a, \qquad \frac{Dv_g}{Dt} = -fu_a$$

[where $D/Dt \equiv \partial/\partial t + (u_g + u_a)\partial/\partial x + (v_g + v_a)\partial/\partial y + w\partial/\partial z$ is the Lagrangian time derivative following the total flow], show that in confluence a near-surface ageostrophic velocity is directed from the anticyclonic to the cyclonic side of the front (e.g., southward ageostrophic flow at the western flank of the eddy C_1; cf. Figs. 8 and 7a), whereas in difluence a near-surface ageostrophic velocity is directed from the cyclonic to the anticyclonic side of the front (e.g., northward ageostrophic flow at the eastern flank of C_1). Each of these near-surface ageostrophic motions is compensated by an ageostrophic flow in the opposite direction at greater depth (Fig. 9), explaining the occurrence of opposing ageostrophic circulations between Figs. 7a and 7b. The resulting ageostrophic divergence/convergence quadrupole causes downwelling ($w < 0$) and vortex stretching ($\partial w/\partial z > 0$) to occur in the surface region downstream of the surface horizontal ageostrophic flow, and upwelling ($w > 0$) and vortex compression ($\partial w/\partial z < 0$) in the surface region upstream. Below the depth of strongest vertical motion, deep vortex stretching is inferred (alongside upwelling) below near-surface vortex compression and, similarly, deep vortex compression is implied (alongside downwelling) below near-surface vortex stretching. As the downstream acceleration of the geostrophic flow occurs in opposite directions if the positions relative to the axis of the front of the cyclonic and the anticyclonic sides are swapped, the induced ageostrophic circulation is reversed from one case to the other. This is conducive to the surface (or deep) horizontal ageostrophic flow being in opposite sense for cyclonic and anticyclonic features. In Fig. 5 and 7, the horizontal ageostrophic flow reinforces the geostrophic current near the surface of anticyclones (e.g., anticyclonic meander of PF jet) and in the deep body of cyclones (e.g., eddy C_1), while opposing the geostrophic flow near the surface of cyclones and in the deep body of anticyclones.

The conceptual model in Fig. 9 complies with the principle of isentropic PV conservation following the flow (Ertel 1941). After Pollard and Regier (1992), isentropic PV can be approximated by isopycnal PV,

$$q^{ip} = N^2 g^{-1}(f + \zeta_g - fF_g),$$

where

$$F_g = N^{-2}[(\partial u_g/\partial z)^2 + (\partial v_g/\partial z)^2]$$

is the geostrophic gradient Froude number and the hydrostatic and geostrophic approximations have been applied. The dominant balance in this expression is between stratification (parameterized by $N^2 g^{-1}$) and vor-

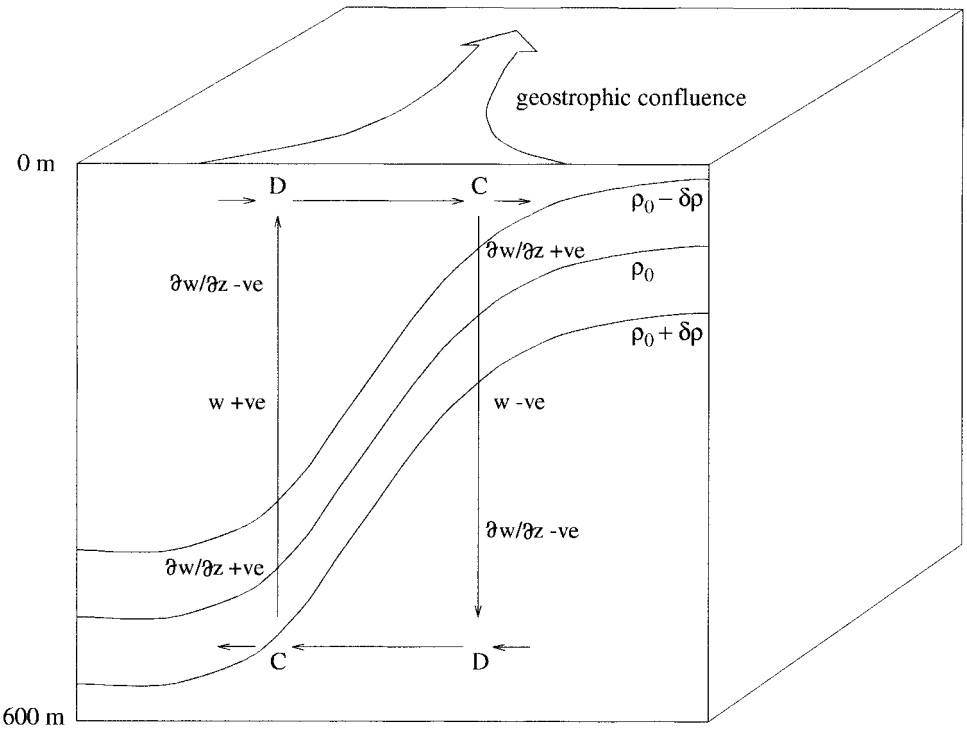

FIG. 9. Idealized model of the ageostrophic circulation in a geostrophic confluence. Three typical isopycnals with potential densities in the range $\rho_0 - \delta\rho$ to $\rho_0 + \delta\rho$ are represented. Regions of convergence and divergence of the ageostrophic flow are indicated by the letters C and D, respectively.

ticity ($f + \zeta_g$). Thus, the acceleration of the geostrophic flow in frontogenetic regions leads to a downstream increase of cyclonic ζ_g on the cyclonic side of the front, accompanied by an increase of anticyclonic ζ_g on the anticyclonic flank. To conserve PV following the geostrophic motion, near-surface vortex stretching (compression) through downwelling (upwelling) is required on the cyclonic (anticyclonic) side, with a near-surface horizontal ageostrophic flow directed from the anticyclonic to the cyclonic flank (and a reversed horizontal ageostrophic flow at greater depth) to conserve mass.

To explore the dynamical implications of the diagnosed circulation, Figs. 10 and 11 present meridional sections across the FSS of the buoyancy advection by the geostrophic and ageostrophic flow, scaled as an equivalent heat advection, $F_h^* = -c_p\alpha_T^{-1}\mathbf{u}\cdot\nabla\rho$, where c_p ($\equiv 4 \times 10^3$ J kg^{-1} K^{-1}) is the specific heat capacity of seawater and α_T ($\equiv 10^{-4}$ K^{-1}) its thermal expansion coefficient. On both the frontogenetic transect in the western flank of the eddy C_1 (10.85°E) and the frontolytic section along its eastern flank (11.33°E) F_h^* has a patchy distribution dominated by the geostrophic component of the buoyancy advection. The confluences and difluences of the geostrophic deformation supplied by the PF jet and the eddy C_1 reflect clearly in the F_h^* field. Along 10.85°E, a geostrophic confluence results in a gain of buoyancy in the lighter (northern) side of the frontal jet and a loss of buoyancy in its denser (southern) side, as observed in Fig. 10a in the form of a pair of fringes of opposite sign (positive near 49.8°S and negative at ~50.2°S, with the core of the jet embedded in between at 50.1°S) below the summer mixed layer. Buoyancy gain is also associated with the weak positive cell near 50.7°S, which, combined with the negative fringe to the north and considering the reversal of isopycnic slopes there, implies frontogenesis in the southwestern periphery of the cyclonic eddy.

Along 11.33°E (Fig. 11a), in contrast, there is a loss of buoyancy in the lighter side of the front and a gain of buoyancy in its denser side, shown as two bands of positive and negative buoyancy advection at 50.4° and 50.1°S, respectively, on either side of the northern flank of the eddy C_1. A weak gain of buoyancy (and acceleration) at the PF jet farther north is however indicated by the positive fringe at 49.8°S in conjunction with the negative band to the south.

Despite the dominant role of the geostrophic advection of buoyancy, the vertical buoyancy advection (Figs. 10b and 11b) is, occasionally, of the same order of magnitude (~1 W m^{-3}) and exerts an appreciable influence on the net buoyancy advection. Positive values in excess of 1 W m^{-3} have been calculated at the depths of the summer and winter pycnoclines in the cyclonic (southern) side of the front on the frontogenetic section, whereas peak negative values of 1–2 W m^{-3} are derived at the same depths on the anticyclonic (northern) margin of the confluence. Following the reversal of the cross-frontal ageostrophic circulation cell, the pattern is re-

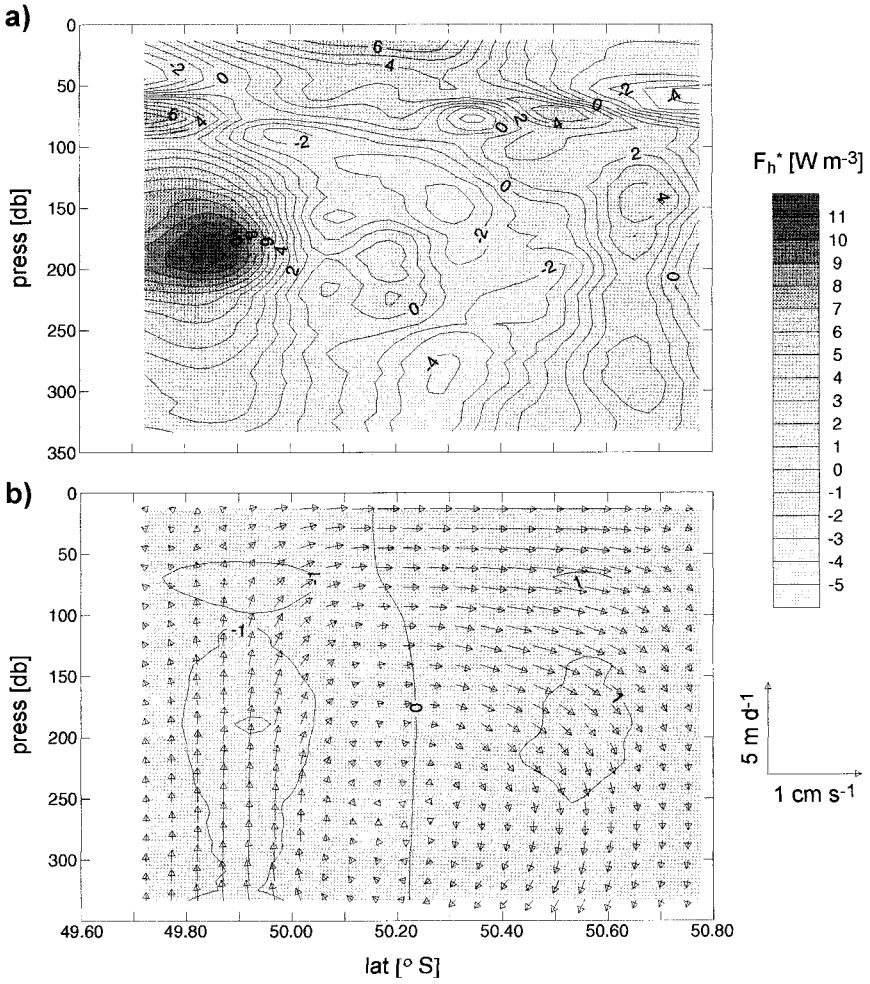

FIG. 10. Vertical distribution on a section crossing the FSS area along 10.85°E of the contribution to the buoyancy advection F_h^* from (a) the geostrophic flow and (b) the ageostrophic flow (shown by arrows). The characteristic uncertainty in the magnitude of F_h^* is estimated as 60%.

versed on the frontolytic section, with a rather large (2–3 W m^{-3}) negative equivalent heat advection on the southern side of the difluence and a weak positive contribution on the northern side.

The crucial property of the vertical buoyancy advection does not reside, however, in its magnitude (which is comparatively small), but rather in its ability to transfer potential energy vertically and thus modify the buoyancy budget of a given depth level. This is in clear contrast to the mere horizontal redistribution of buoyancy effected by the geostrophic flow. In the ability to alter the buoyancy reservoir at a particular depth, the vertical buoyancy transfer driven by the ageostrophic flow is in competition with atmospheric buoyancy forcing, with the distinction that the former is an adiabatic process. This resemblance is not trivial and underlies the belief that oceanic subduction is strictly driven by buoyancy transfer mechanisms of either nature (Nurser and Marshall 1991; Marshall et al. 1993; Follows and Marshall 1994; Spall 1995; Rudnick 1996).

To this respect, Figs. 12 and 13 display the field of the variable $G_b^z = -\rho_0^{-1} g\, w'\, \rho'$ along each of the sections, where w' and ρ' are defined as the deviations of w and ρ from their areal mean values at each depth. Here G_b^z can be thought of as the rate of baroclinic conversion of potential to kinetic energy. On the frontogenetic section (Fig. 12), a positive baroclinic conversion is suggested throughout, reaching values of more than 10 $cm^2\ s^{-2}\ d^{-1}$ below the winter pycnocline and 2–4 $cm^2\ s^{-2}\ d^{-1}$ at the summer mixed layer. Peak magnitudes are attained at the main upwelling and downwelling sites, their positive sign being indicative of lighter water upwelling near 49.9°S and denser water sinking at ~50.5°S. Conversely, on the frontolytic section (Fig. 13), a negative conversion (of as much as 27 $cm^2\ s^{-2}\ d^{-1}$ below the winter pycnocline and 6 $cm^2\ s^{-2}\ d^{-1}$ within the mixed layer) is generally implied, with shoaling denser water and downwelling lighter water.

In a (frontogenetic) geostrophic confluence, a positive baroclinic conversion must require a flattening of the

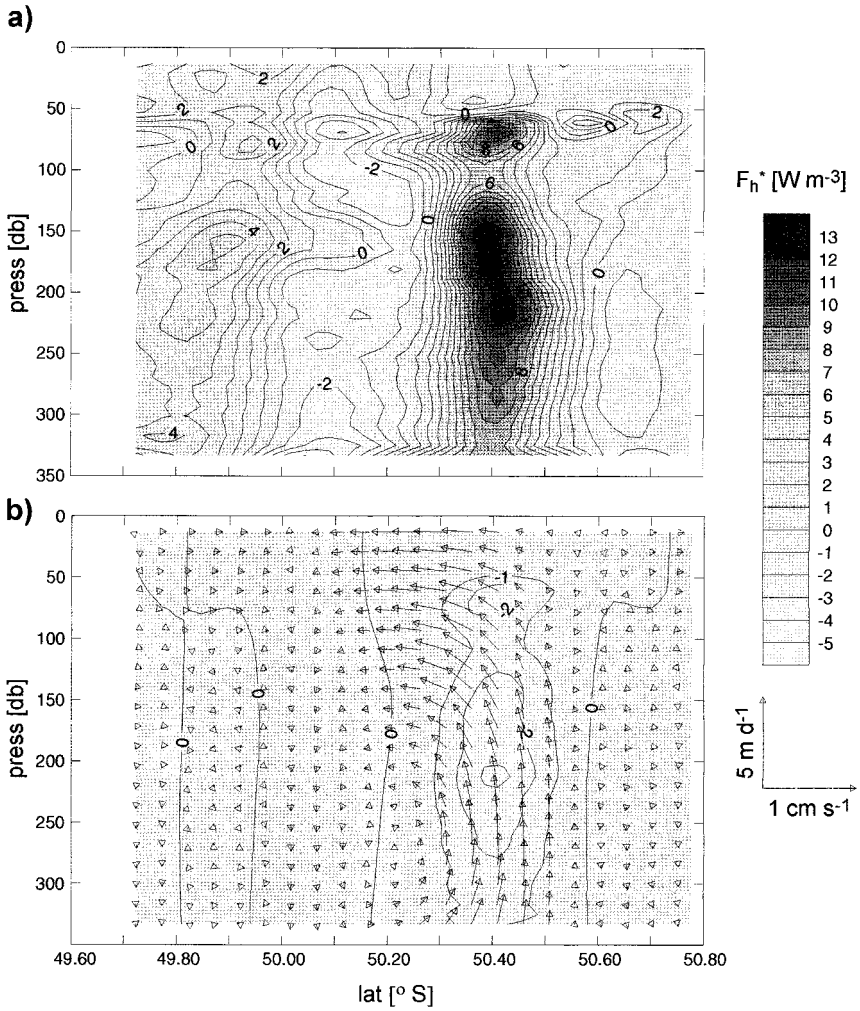

FIG. 11. As in Fig. 10 but for a section crossing the FSS area along 11.33°E.

isopycnals and frontolysis. This is the mechanism necessary for converting available potential energy (APE) to EKE (as required for the growth of baroclinically unstable disturbances) as water parcels are advected into the frontal jet. In contrast, a (frontolytic) geostrophic difluence would be associated with a negative conversion leading to an enhancement of frontal isopycnic slopes and frontogenesis. The result would be a conversion of EKE to APE (in opposition to the requirements of baroclinic instability) as water parcels approach the difluence from upstream and the frontal jet decelerates. It is thus shown that two scenarios are encountered along a frontal jet that effect either the kind of energy conversion implicit in baroclinic instability or the opposite.

Numerical studies of baroclinically unstable waves growing on a frontal jet (Wang 1993; Spall 1995, 1997) have suggested however that the frontal-mean ageostrophic circulation cell (the residual ageostrophic circulation cell averaged over at least one periodic structure of the meandering front) is likely to be very different from the instantaneous ageostrophic circulation at any one frontal location, and that in consequence it is unfeasible to infer the properties of this integrated cell (and the energy conversion implied) from single cross-frontal sections. To detect the buoyancy flux linked to the frontal-mean ageostrophic circulation, Fig. 14 presents a profile of the mean and standard deviation of G_b^z corresponding to the entire domain of the FSS. A net positive baroclinic conversion is calculated at every depth, peaking in the vicinity of 280 m with a value in excess of 1.2 cm^2 s^{-2} d^{-1} (which, according to the *t*-test, is statistically different from zero with 95% confidence). The sign of this flux is indeed in accord with the slumping of isopycnals linked to the process of baroclinic instability. However, it is not strictly clear that the physical significance of this estimate is sufficient. It could be argued that, since the outcome of the average is the residual of the addition of two large contributions with opposite sign, the result of the calculation depends critically on whether or not an integer number of meander wavelengths was encompassed by the survey. It

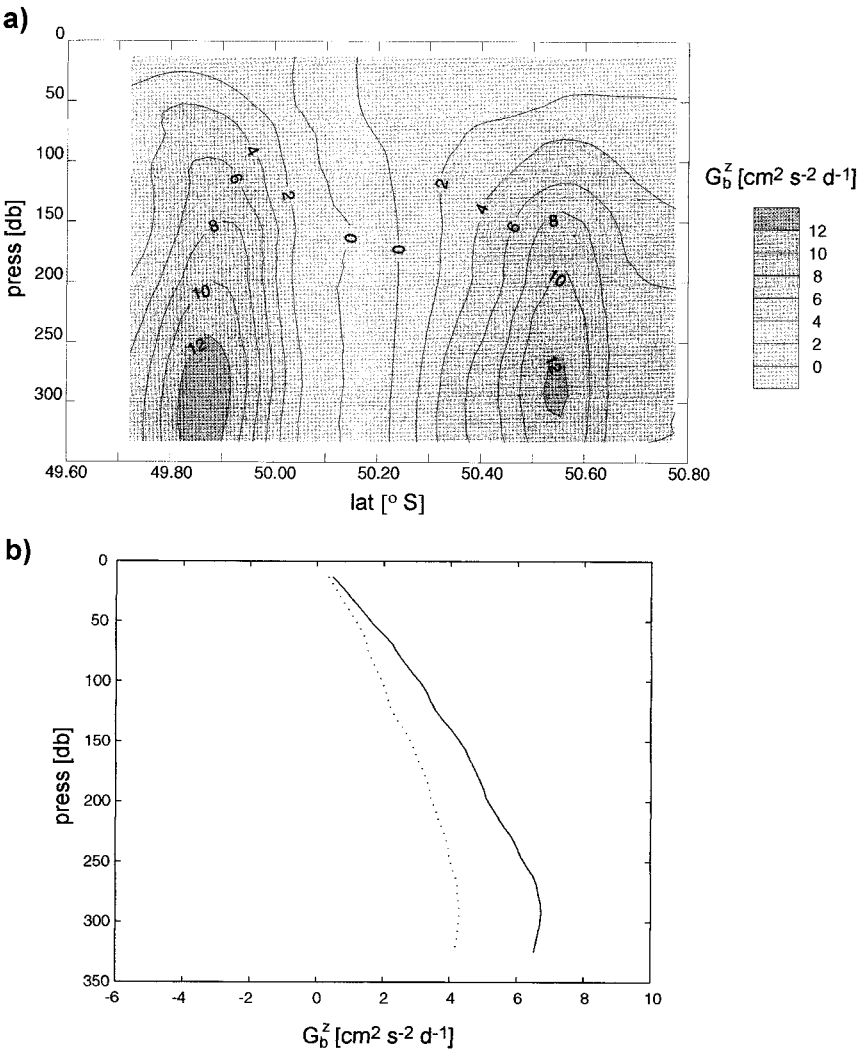

FIG. 12. (a) Vertical distribution of the baroclinic conversion rate G_b^z on a section crossing the FSS area along 10.85°E, with (b) showing profiles of the mean G_b^z (solid line) and the rms deviation of G_b^z (dotted) on the section. The characteristic uncertainty in the magnitude of G_b^z is estimated as 50%.

is nevertheless reassuring that the FSS comprised two entire periodic structures almost exactly (Fig. 3b): one linked to the PF jet flowing east along ~50.2°S, the other involving the cyclonic eddy C_1 and the weak cyclonic meander at the southwest of the FSS.

Independent support for the positive baroclinic conversion in Fig. 14 may be extracted from the q^{ip} field of the FSS, where q^{ip} variability occurs principally with depth (Fig. 15) and is dominated by changes in the stratification term $g^{-1}N^2$. Relative minima in the absolute value of q^{ip} are observed in the uppermost 30–40 m ($q^{ip} \sim -0.10 \times 10^{-9}$ m^{-1} s^{-1}), corresponding to the mixed layer above the summer pycnocline, and in the depth range 90–140 m ($q^{ip} \sim -0.15 \times 10^{-9}$ m^{-1} s^{-1}), associated with the layer of high isopycnic thickness bounded by the summer pycnocline above and the winter pycnocline below. Relative maxima in the absolute value of q^{ip} occur at the summer ($q^{ip} \sim -0.50 \times 10^{-9}$ m^{-1} s^{-1}) and winter ($q^{ip} \sim -0.25 \times 10^{-9}$ m^{-1} s^{-1}) pycnoclines, coinciding with peaks in stratification.

The energy conversion occurring during baroclinic instability is linked to an Eliassen–Palm flux or ''bolus'' transport of water across the front. Conventionally parameterized by the bolus velocity $v^* = (1/\overline{h})\,\overline{h'v'}$ (e.g., Lee et al. 1997), where overbars represent a mean over several spatial or temporal periods and primes denote deviations from this mean, the bolus transport can be regarded as a residual water mass transfer arising from the correlation between the velocity of parcels of that particular water mass and their isopycnic thickness h. Its correlation with gradients of q^{ip} in numerical simulations of an unstable jet (Lee et al. 1997; Marshall et al. 1999) is used here to infer its properties in the FSS. The implicit assumption that time-averaged model behavior is a reliable indicator of synoptic processes in the ocean might seem pretentious, and invites to caution

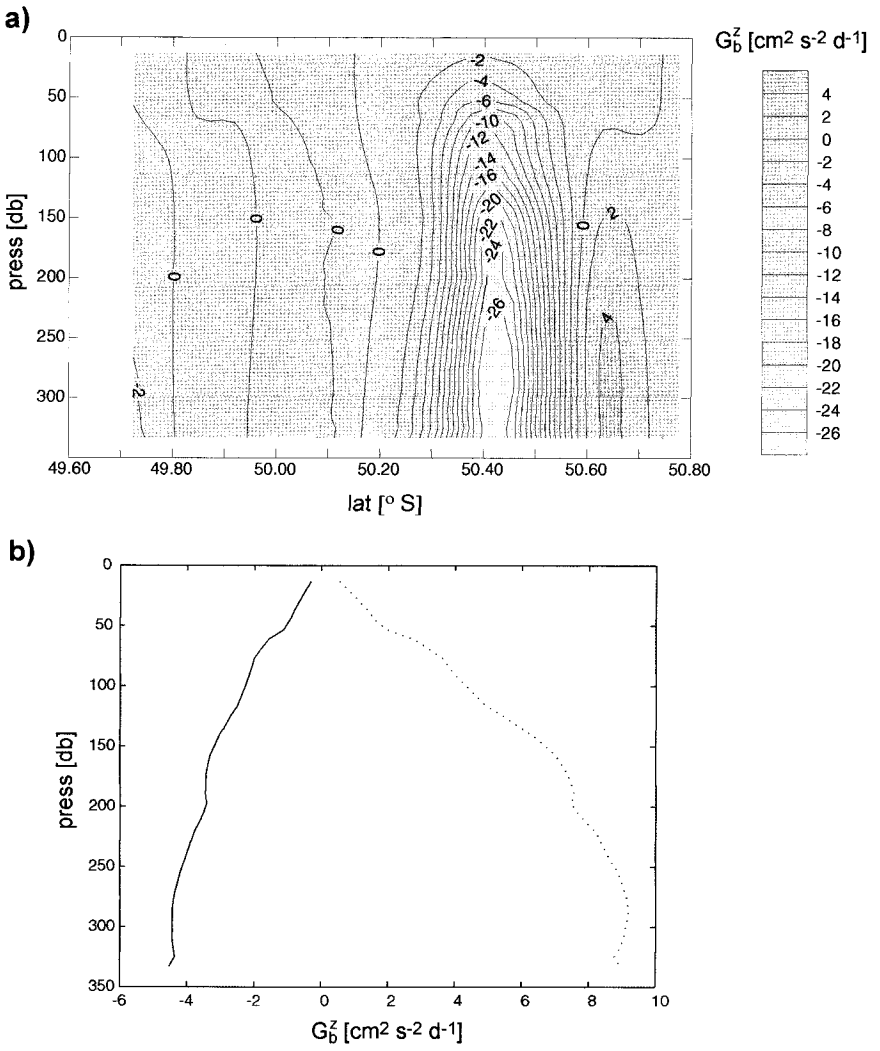

FIG. 13. As in Fig. 12 but for a section crossing the FSS area along 11.33°E.

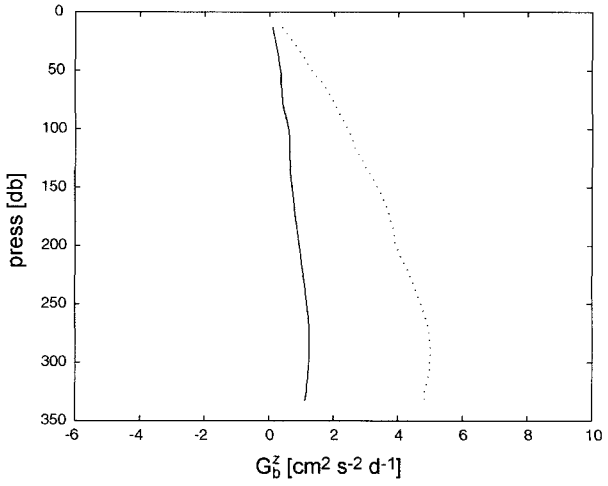

FIG. 14. Profiles of the mean G_b^z (solid line) and the rms deviation of G_b^z (dotted) averaged areally over the FSS. The characteristic uncertainty in the magnitude of the areal mean G_b^z is estimated as 20%.

in considering the results of the exercise. Some reassurance is nevertheless provided by the stratification of the PF region being essentially unchanged during the summer months, which comprise a number of baroclinic life cycles.

Figure 16a presents the isopycnic distribution of q^{ip} along a meridional transect crossing the PF region. The ideas above predict that, for isopycnals below $\sigma_0 \sim 27.20$ kg m^{-3}, the successive cross-frontal ageostrophic circulation cells will on average flux a greater volume of fluid southward, for the water present on the northern side of the front at this isopycnic range has greater thickness. Likewise, there will be a net northward bolus transport of the water bounded by the isopycnals $\sigma_0 \sim 27.05$ and $\sigma_0 \sim 27.20$ kg m^{-3} and a southward bolus transport above $\sigma_0 \sim 27.05$ kg m^{-3}. Strictly speaking, these predictions should only refer to the northern border of the cyclonic eddy and the surveyed area to the north. On the southern flank of the eddy the slope of the q^{ip} con-

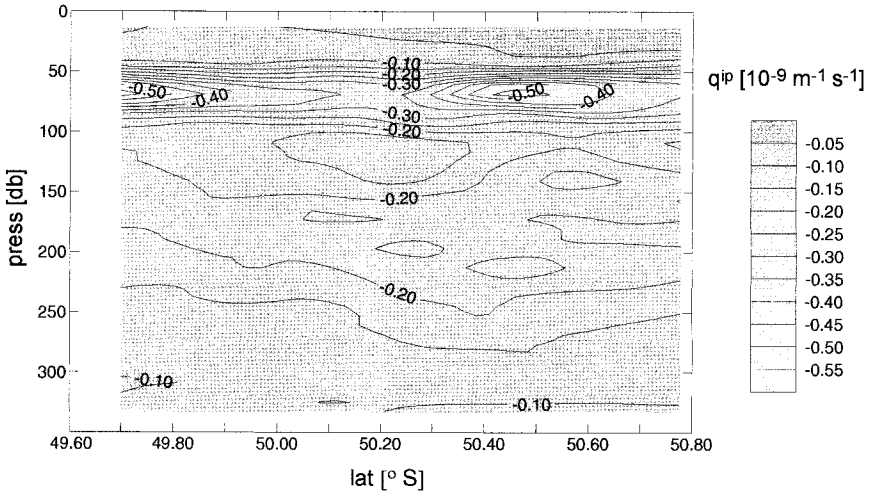

FIG. 15. Vertical distribution of q^{ip} on a section crossing the FSS area along 10.85°E. The characteristic uncertainty in the magnitude of q^{ip} is estimated as 10%.

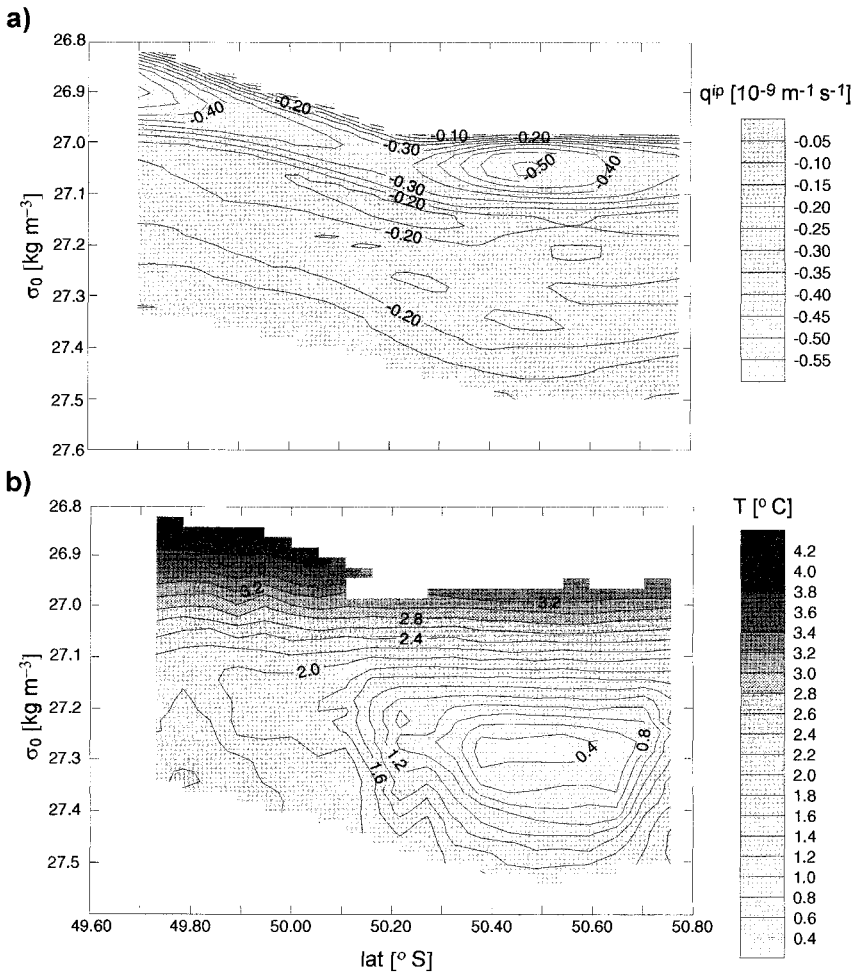

FIG. 16. Isopycnic distributions of (a) q^{ip} and (b) temperature on a section crossing the FSS area along 10.85°E.

tours in Fig. 16a reverses and the same criteria no longer apply.

Figure 16b, displaying T along the same section, broadly supports the vertical profile of the bolus transport inferred above. Thus, the T-min of WW seems to propagate north preferentially along isopycnals in the range $\sigma_0 \sim 27.10$–27.20 kg m^{-3}, whereas for greater densities warmer water from the northern side of the PF intrudes south along $\sigma_0 \sim 27.30$ kg m^{-3}. Isopycnals above $\sigma_0 \sim 27.05$ kg m^{-3} are however embedded in the mixed layer and their isopycnal PV is modified by solar warming and air–sea interaction. Though in these circumstances the principle of isentropic PV conservation no longer applies strictly, there are indications that the tendency is for a near-surface southward bolus transport to exist. These are provided by the detection, during the Long Transect and the CSS earlier in the heating season, of a clear southward intrusion of warmer water from north of the PF directly above the northern boundary of the WW that is suggestive of such a transport (Strass et al.).

We thus propose that the q^{ip} field in the PF region is consistent with a bolus transport across the front that fluxes light water southward near the surface and denser water northward at the depth of the capped-off WW. The reduction in isopycnic slopes and APE release associated with this residual transport are symptomatic of the occurrence of baroclinic instability and take a different expression in the net upward buoyancy flux (positive G_b^z) shown in Fig. 14. Furthermore, because the ageostrophic cross-front circulations that lead to the bolus transport conserve potential density and the frontal isopycnic slopes must remain in a long-term equilibrated state, the tendency must be for the T-min to flow north along deepening isopycnals, resulting in an intrusion into the winter pycnocline and a net subduction of the capped-off WW. This does not imply, however, that the observed northward protrusion of the T-min layer must be exactly isopycnic at any time (Fig. 16b displays several examples of diapycnic thermal intrusions). As recognized by Woods et al. (1986) and Onken et al. (1990), thermohaline intrusions created isopycnally at a front may appear to slope across isopycnals as a result of differential advection along density surfaces.

Were it to be assumed that the baroclinic conversion rate in Fig. 14 and the geometry of the frontal potential density field are representative of a longer-term steady state, a rate of subduction could be estimated. Taking the vertical derivative of G_b^z in Fig. 14 yields a mean upward buoyancy advection at the FSS of $\sim 5 \times 10^{-5}$ cm s^{-2} d^{-1} (e.g., G_b^z increases from 0 at the surface to 1 cm^2 s^{-2} d^{-1} at 200 m), corresponding to a downward mass advection of $\sim 5 \times 10^{-5}$ kg m^{-3} d^{-1} after scaling by $-g\rho_0^{-1}$; dividing this figure by the observed vertical potential density gradient near the level of the winter pycnocline ($\sim 10^{-3}$ kg m^{-4}, e.g., the spacing between the $\sigma_0 = 27.10$ kg m^{-3} and $\sigma_0 = 27.20$ kg m^{-3} isopycnals is typically $\sim$100 m), an approximate subduction rate of $\sim$0.05 m d^{-1} (or $\sim$20 m yr^{-1}) is obtained; combined with a characteristic isopycnic slope across the frontal region of $\sim 2 \times 10^{-4}$ this subduction rate implies a meridional progression of the WW along isopycnals at $\sim$0.3 cm s^{-1}. A number of simplifications are implicit in this calculation and the resulting figures can only be considered representative to within an order of magnitude. It is encouraging to note though that the rate of northward progression of the T-min layer calculated above is a factor of 4 smaller than, but of comparable magnitude to, that of a parcel of WW that was inferred by Strass et al. from comparison of two transects across the CSS region performed two weeks apart.

6. Summary and conclusions

We have shown, through an analysis of the velocity and isopycnal PV fields in the PF region, that the ageostrophic circulation induced by baroclinic instability leads to a time-mean subduction of water from the south that becomes a northward protrusion of the T-min of WW. The subduction process involves a time-mean slumping of isopycnals that, in the absence of external forcing, would lead to the demise of the steep isopycnic slopes that characterize the PF region. The potential importance of this frontolytic role of baroclinic instability for the understanding of the nature of ocean fronts had already been recognized by Spall (1997) in a numerical study of the evolution of an unstable baroclinic frontal jet in a large-scale deformation field.

Mesoscale subduction at the PF is not a seasonal phenomenon but occurs throughout the year, as can be inferred from the persistence of the northward protrusion of WW in the region during the cooling season (Strass et al.). In Section 5, we estimated a mesoscale subduction rate of $O(20$ m yr$^{-1})$, comparable in magnitude to the rates associated with the mean, gyre-scale circulation (Marshall et al. 1993). This is in support of the predictions of numerical models of frontal and eddy-driven subduction (Follows and Marshall 1994; Marshall 1997; Spall 1997). As concerns the geographical extent of the process, it is believed to be such that a circumpolarly valid criterion for pinpointing the position of the PF has been developed in terms of the northern boundary of the subsurface T-min of WW (Belkin and Gordon 1996). Indeed, the possibility of a northward export of WW in the PF region through cross-frontal exchanges and its circumpolar involvement in the formation of Antarctic Intermediate Water at the Subantarctic Front farther north has been the subject of speculation by a number of authors (e.g., Sievers and Nowlin 1984). We show in this work that such a cross frontal exchange can be feasibly driven by baroclinic instability in the region.

We further propose that mesoscale subduction, as described here, is not exclusive to the PF but applies to the other frontal regions of the Southern Ocean. This may be illustrated by Fig. 17, showing the Sverdrupian isopycnal PV ($q_{\mathrm{Sv}} = N^2 g^{-1} f$) distribution on potential

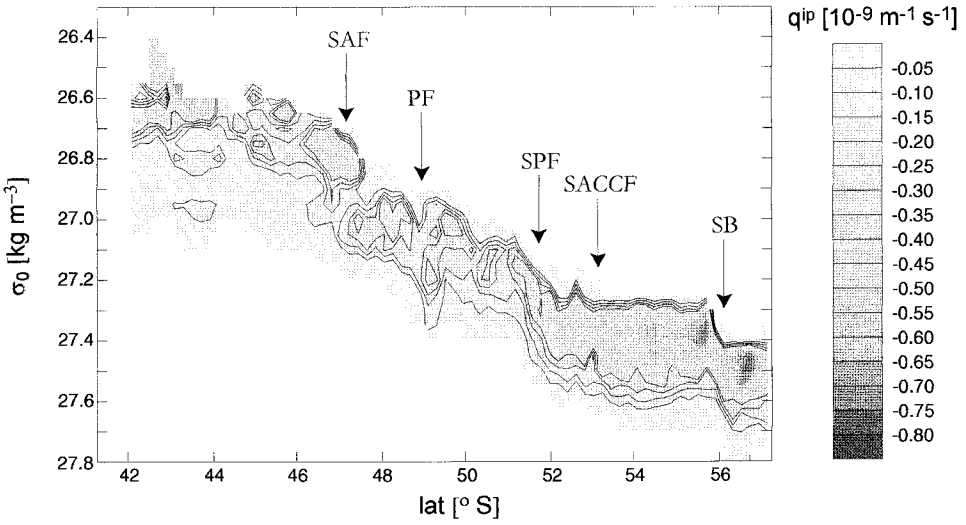

FIG. 17. Isopycnic distribution of q_{Sv} along the Long Transect. The contours in the range -0.30×10^{-9} to -0.15×10^{-9} m^{-1} s^{-1} are marked by solid lines. The positions of the frontal features crossed during the long Transect are indicated on the upper axis: SAF (Subantarctic Front), PF (Polar Front), SPF (Southerly Polar Front), SACCF (Southern ACC Front), and SB (Southern Boundary of the ACC).

density surfaces along the Long Transect. Four of the five sites at which the layers of high stratification slope most steeply [giving rise to the greatest likelihood for the occurrence of depth reversals of the isopycnal q^{ip} gradient (IPVG)] coincide with the positions of commonly reported circumpolar frontal features (the other is linked to the SPF). Depth reversal of the IPVG is a necessary condition for the onset of baroclinic instability (e.g., Pedlosky 1987). Without this, it would be physically impossible to release APE through a cross-front bolus transport cell, as seen in section 5. IPVG reversals occur at fronts due to a superposition of the enhanced frontal isopycnic slopes and an essentially flat pycnocline linked to the uniformity of atmospheric forcing across each frontal region. Given that the basic structure of the upper-ocean IPV field (and, predictably, the profile of the bolus transport) is shared, the description of mesoscale subduction presented here should broadly apply at all fronts.

The issue remains to be addressed as to what frontogenetic process may balance the frontolytic action of baroclinic instability at the PF, thereby maintaining the frontal region in a long-term steady state. In section 5, we identified a frontogenetic (frontolytic) site in a region of confluence (difluence) of the geostrophic flow associated with the PF jet and an eddy. The ability of transient features to either supply momentum to or decelerate the mean flow is a common observation in numerical models (e.g., Ivchenko et al. 1996; Stevens and Ivchenko 1997; Dijkstra and van der Vaart 1998; Best 1999) and altimetric studies of the ACC (Johnson et al. 1992; Morrow et al. 1992). Though the sign of the circumpolarly averaged Reynolds stress within the ACC is still a matter of controversy, the generally accepted theoretical view (e.g., Hoskins 1982) is that at length scales larger than the Rossby radius of deformation [~15 km in the ACC (Inoue 1985)] the net effect of baroclinic instability is to feed momentum back into the mean flow. This is an integral part of the instability process at its nonlinear stage and translates into a sharpening of fronts by the eddies evolving from the linear stage of the instability. As revealed in section 5, the extent of this sharpening is ultimately limited by the frontolytic action of the time-mean ageostrophic circulation at length scales smaller than the Rossby radius.

Being intrinsically related to the baroclinic instability process, mesoscale eddy activity cannot be regarded as an original source of APE, but rather as an important agent feeding back momentum into the mean flow. Observational and numerical evidence to date (e.g., Deacon 1982; Kazmin and Rienecker 1996) suggests that the APE reservoir of the ACC, the Southern Ocean fronts, and the PF region in particular is originally supplied by a combination of the large-scale frontogenetic processes (Ekman convergence, Ekman advection, Ekman pumping, and thermohaline forcing at the ocean surface). The resulting competition between a large-scale frontogenesis and a mesoscale frontolysis leads to a dichotomy of length scales that may, arguably, be fundamental in understanding the zonation of the ACC. A simplistic conceptual model linking the latter to the former can indeed be developed in the frame of the theory of geostrophic turbulence.

The key point in this model may be sketched by approximating the IPVG as

$$\frac{\partial}{\partial y}\left(\frac{f}{h}\right) = \frac{\beta}{h} - \frac{f}{h^2}\frac{\partial h}{\partial y}, \tag{3}$$

where the contribution of relative vorticity has been neglected. The rhs of Eq. (3) shows that the meridional gradient of the isopycnic thickness ($\partial h/\partial y$) is the only

quantity liable to reverse sign with depth, and hence an excessive size of the term β/h would effectively prevent the IPVG from doing so. It is thus appreciated that the onset of baroclinic instability can be impeded by the spherical shape of the earth when meridional excursions of water parcels are sufficiently ample to notice it [i.e., at length scales larger than the Rhines scale $\sim$200 km in the ACC (Naveira Garabato 1999)]. Thus, if baroclinic instability in the Southern Ocean occurs preferentially at the fronts (as hinted in Fig. 17), the frontolytic opposition of the process to the large-scale frontogenesis will tend to be confined to frontal regions by planetary curvature. This confinement is entirely analogous to the existence of an upper bound to the migration of dominant eddies toward large scales in a turbulent eddy field (Rhines 1975), and is conducive to a concentration of the APE produced by the large-scale frontogenesis at fronts, which act as regions of maximum APE dissipation.

Despite its partly speculative character, the ideas proposed here are in accord with the results of Treguier and Panetta (1994) in a quasigeostrophic β-plane channel model of the ACC. They showed that, though the frontal jets were occasionally steered by topography and strongly constrained by the curvature of the meridional wind stress profile, the circumpolar continuity of the fronts was exclusively attributable to transient eddy fluxes. Our conclusions lend support to the findings of Marshall and Adcock (1998) who, in a similar numerical experiment, obtained a stepwise meridional PV distribution with zonal frontal jets separating regions of uniform PV that is reminiscent of the observations in Fig. 17. They noted that the spacing between the jets was of the order of the Rhines scale and suggested that planetary control of the meridional length scale of the baroclinic instability of the jets was responsible for the zonation of the current.

Acknowledgments. The authors are grateful to the officers and crew of PFS *Polarstern* for their ever willing assistance in the collection of the ANT XIII/2 dataset. ACNG thankfully acknowledges the support of the University of Liverpool under a Ph.D. studentship. VHS and HL received support for travel from the British Council and the Deutscher Akademischer Austauschdienst. This study benefited from the comments of two anonymous reviewers, to whom we extend our gratitude.

APPENDIX

Sensitivity of the Diagnostics

We conducted a range of tests to examine the sensitivity of the diagnosed w field to various sources of error. To test for the effect of instrumental errors and internal wave contamination in the density and velocity measurements, we added random noise of prescribed amplitude (± 0.01 kg m^{-1} and ± 0.04 m s^{-1}) to each of the measured fields separately and averaged the resulting perturbations to the w field over five realizations of the noise. An analogous approach was adopted to quantify the error introduced by residual inertial and tidal signals possibly left over from the measured flow (by adding a time-varying sinusoidal current field of 0.04 m s^{-1} amplitude, inertial period, and confined to the mixed layer and another of 0.02 m s^{-1} amplitude, semidiurnal period, and barotropic to the measured velocity field).

TABLE A1. Characteristic uncertainty in the magnitude of w (as diagnosed by the SG omega equation) induced by different error sources.

Error source	Magnitude of error
Noise in ρ and (u_g, v_g) data	5%
Spatial resolution and scales of gridding	40%
Neumann lateral boundary conditions	5%
Dirichlet bottom boundary conditions	35%
Neglect of β effect	1%
Assumption of synopticity	Negligible

The influence of the spatial resolution of the survey and the scales of gridding on the diagnosed vertical flow was inspected by varying d_x and d_y by 10% of their initial values. Quantifying the error introduced by the assumption of Neumann lateral boundary conditions involved setting the gradient of w perpendicular to the boundary to Gaussian noise of ± 0.6 m d^{-1} km^{-1} amplitude and spatially correlated over e-folding length scales of 20 km in the horizontal and 50 m in the vertical (again averaging perturbations to the w field over five realizations of the noise). Similarly, testing the sensitivity of the solution to the bottom boundary condition was attempted by setting the vertical velocity at 600 m to Gaussian noise of ± 1 m day^{-1} amplitude and horizontally correlated over an e-folding length scale of 20 km.

The above sensitivity experiments showed that the spatial patterns and signs in our diagnosed vertical velocity and buoyancy flux fields are robust features. The different error sources, however, affected the magnitude of the vertical motions/fluxes substantially. The uncertainty in the magnitude of w introduced by each error source is given in Table A1.

The error implicit in the neglect of the β effect in the SG omega equation was estimated by solving the quasigeostrophic version with and without the β effect. Though rather inhomogenously distributed, this was found to be minimal (Table A1). The effect of the assumption of synopticity implicit in the SG omega equation was presumed negligible. As shown by Strass et al. (2000) from a 1-yr length record of mooring velocities, our survey of the PF was carried out during a highly steady period. This can also be appreciated from the remarkable similarity between hydrographic data collected in the FSS area during the CSS and the FSS,

which were conducted on average one week apart (cf. Figs. 3a and 3b).

An estimate of the total uncertainty in the magnitude of w (50%) was computed (assuming that the errors induced by different sources are independent) by adding the errors from the various sources in Table 1 in quadrature. Identical techniques were used to calculate the characteristic uncertainties in the magnitude of the other derived physical quantities: u_g and v_g (5%), ζ_g and q^{ip} (10%), u_a and v_a (35%), G_b^z (50%), and F_{Ho} and F_h^* (60%).

REFERENCES

Allen, J. T., and D. Smeed, 1996: Potential vorticity and vertical velocity at the Iceland–Færœs front. *J. Phys. Oceanogr.,* **26,** 2611–2634.

Belkin, I. M., and A. L. Gordon, 1996: Southern Ocean front from the Greenwich meridian to Tasmania. *J. Geophys. Res.*, **101,** 3675–3696.

Best, S. E., V. O. Ivchenko, K. J. Richards, R. D. Smith, and R. C. Malone, 1999: Eddies in numerical models of the Antarctic Circumpolar Current and their influence on the mean flow. *J. Phys. Oceanogr.,* **29,** 328–350.

Botnikov, V. N., 1963: Geographical position of the Antarctic Convergence zone in the Southern Ocean (in Russian). *Sov. Antarct. Exped. Inf. Bull.*, Engl. transl., **4,** 324–327.

Chelton, D. B., M. G. Schlax, D. L. Witter, and J. G. Richman, 1990: Geosat altimeter observations of the surface circulation of the Southern Ocean. *J. Geophys. Res.,* **95,** 17 877–17 904.

Deacon, G. E. R., 1982: Physical and biological zonation in the Southern Ocean. *Deep-Sea Res.,* **29,** 1–15.

Dewar, W. K., and J. C. Marshall, 1994: Inertial embedded fronts. *J. Phys. Oceanogr.*, **24,** 79–90.

Dijkstra, H. A., and P. C. F. van der Vaart, 1998: On the physics of upgradient momentum transport in unstable eastward jets. *Geophys. Astrophys. Fluid Dyn.,* **88,** 295–325.

Ertel, H., 1941: Ein neuer hydrodynamischer Wirbelsatz. *Meteor. Z.,* **59,** 271–281.

Fiekas, V., H. Leach, K. J. Mirbach, and J. D. Woods, 1994: Mesoscale instability and upwelling. Part 1: Observations at the North Atlantic intergyre front. *J. Phys. Oceanogr.,* **24,** 1750–1758.

Follows, M. J., and J. C. Marshall, 1994: Eddy driven exchange at ocean fronts. *Ocean Modelling* (unpublished manuscripts), **102,** 5–9.

Gill, A. E., 1982: *Atmosphere-Ocean Dynamics.* Academic Press, 662 pp.

Gille, S. T., 1997: The Southern Ocean momentum balance: Evidence for topographic effects from numerical model output and altimeter data. *J. Phys. Oceanogr.,* **27,** 2219–2232.

Holliday, N. P., and J. F. Read, 1998: Surface oceanic fronts between Africa and Antarctica. *Deep-Sea Res.,* **45,** 217–238.

Holton, J. R., 1978: *An Introduction to Dynamic Meteorology.* Academic Press, 511 pp.

Hoskins, B. J., 1975: The geostrophic momentum approximation and the semi-geostrophic equations. *J. Atmos. Sci.,* **32,** 233–242.

——, 1982: The mathematical theory of frontogenesis. *Annu. Rev. Fluid Mech.,* **14,** 131–151.

——, and I. Draghici, 1977: The forcing of ageostrophic motion according to the semi-geostrophic equations and in an isentropic coordinate model. *J. Atmos. Sci.,* **34,** 1859–1867.

——, ——, and H. C. Davies, 1978: A new look at the ω-equation. *Quart. J. Roy. Meteor. Soc.,* **104,** 31–38.

Hughes, C. W., and P. D. Killworth, 1995: Effects of bottom topography in the large-scale circulation of the Southern Ocean. *J. Phys. Oceanogr.,* **25,** 2485–2497.

——, M. S. Jones, and S. Carnochan, 1998: Use of transient features to identify eastward currents in the Southern Ocean. *J. Geophys. Res.,* **103,** 2929–2943.

Inoue, M., 1985: Modal decomposition of the low-frequency currents and baroclinic instability at Drake Passage. *J. Phys. Oceanogr.,* **15,** 1157–1181.

Ivchenko, V. O., K. J. Richards, and D. P. Stevens, 1996: The dynamics of the Antarctic Circumpolar Current. *J. Phys. Oceanogr.,* **26,** 753–774.

——, A. M. Treguier, and S. E. Best, 1997: A kinetic energy budget and internal instabilities in the Fine Resolution Antarctic Model. *J. Phys. Oceanogr.,* **27,** 5–22.

Johnson, G. C., and H. L. Bryden, 1989: On the size of the Antarctic Circumpolar Current. *Deep-Sea Res.,* **36,** 39–53.

Johnson, T. J., R. H. Stewart, C. K. Shum, and B. D. Tapley, 1992: Distribution of Reynolds stress carried by mesoscale variability in the Antarctic Circumpolar Current. *Geophys. Res. Lett.,* **19,** 1379–1382.

Kantha, L. H., 1995: Barotropic tides in the global oceans from a nonlinear tidal model assimilating altimetric tides 1. Model description and results. *J. Geophys. Res.,* **100,** 25 283–25 308.

Kazmin, A. S., and M. M. Rienecker, 1996: Variability and frontogenesis in the large-scale oceanic frontal zones. *J. Geophys. Res.,* **101,** 907–921.

Leach, H., 1987: The diagnosis of synoptic-scale vertical motion in the seasonal thermocline. *Deep-Sea Res.,* **34,** 2005–2017.

Lee, M.-M., D. P. Marshall, and R. G. Williams, 1997: On the eddy transfer of tracers: Advective or diffusive? *J. Mar. Res.,* **3,** 483–505.

Lutjeharms, J. R. E., and H. R. Valentine, 1984: Southern Ocean thermal fronts south of Africa. *Deep-Sea Res.,* **31,** 1461–1475.

——, and ——, 1988: Eddies at the sub-tropical convergence south of Africa. *J. Phys. Oceanogr.,* **18,** 761–774.

Marshall, D., 1997: Subduction of water masses in an eddying ocean. *J. Mar. Res.,* **55,** 201–222.

——, and S. Adcock, 1998: On the formation of inertial jets within the Antarctic Circumpolar Current. *UK Oceanography '98 Programme and Abstracts,* Challenger Society for Marine Science, p. 45.

——, R. G. Williams, and M.-M. Lee, 1999: The relation between eddy-induced transport and isopycnic gradients of potential vorticity. *J. Phys. Oceanogr.,* **29,** 1571–1578.

Marshall, J. C., A. J. G. Nurser, and R. G. Williams, 1993: Inferring the subduction rate and period over the North Atlantic. *J. Phys. Oceanogr.,* **23,** 1315–1329.

Morrow, R., J. Church, R. Coleman, D. Chelton, and N. White, 1992: Eddy momentum flux and its contribution to the Southern Ocean momentum balance. *Nature,* **357,** 482–484.

Mosby, H., 1934: The waters of the Atlantic Antarctic Ocean. *Sci. Results Norw. Antarct. Exped.,* **11,** 1–131.

Naveira Garabato, A. C., 1999: On the physical controls of the biological uptake of CO_2 in the Antarctic Circumpolar Current. Ph.D. dissertation, University of Liverpool, 201 pp.

——, V. H. Strass, and G. Kattner, 2000: Fluxes of nutrients in a three-dimensional meander structure of the Antarctic Polar Front. *Deep-Sea Res. II,* in press.

Nowlin, W. D., Jr., and J. M. Klinck, 1986: The physics of the Antarctic Circumpolar Current. *Rev. Geophys.,* **24,** 469–491.

Nurser, A. J. G., and J. C. Marshall, 1991: On the relationship between subduction rates and diabatic forcing of the mixed layer. *J. Phys. Oceanogr.,* **21,** 1793–1802.

Onken, R., J. Fischer, and J. D. Woods, 1990: Thermohaline finestructure and its relation to frontogenesis dynamics. *J. Phys. Oceanogr.,* **20,** 1379–1394.

Orsi, A. H., T. Whitworth III, and W. D. Nowlin Jr., 1995: On the meridional extent and fronts of the Antarctic Circumpolar Current. *Deep-Sea Res.,* **42,** 641–673.

Park, Y. H., and L. Gambéroni, 1997: Cross-frontal exchange of Antarctic Intermediate Water and Antarctic Bottom Water in the Crozet Basin. *Deep-Sea Res. II,* **44,** 963–986.

Pedlosky, J., 1987: *Geophysical Fluid Dynamics.* Springer-Verlag, 710 pp.

Peterson, R. G., and T. Whitworth III, 1989: The Subantarctic and Polar Fronts in relation to deep water masses through the southwestern Atlantic. *J. Geophys. Res.,* **94,** 10 817–10 838.

Pinot, J.-M., J. Tintoré, and D. P. Wang, 1996: A study of the omega equation for diagnosing vertical motions at ocean fronts. *J. Mar. Res.,* **54,** 239–259.

Pollard, R. T., and L. A. Regier, 1992: Vorticity and vertical circulation at an ocean front. *J. Phys. Oceanogr.,* **22,** 609–625.

Rhines, P. B., 1975: Waves and turbulence on a β-plane. *J. Fluid Mech.,* **69,** 417–443.

——, 1979: Geostrophic turbulence. *Annu. Rev. Fluid Mech.,* **11,** 401–441.

Rintoul, S. R., J. R. Donguy, and D. H. Roemmich, 1997: Seasonal evolution of upper ocean thermal structure between Tasmania and Antarctica. *Deep-Sea Res.,* **44,** 1185–1202.

Rudnick, D. L., 1996: Intensive surveys of the Azores Front. 2: Inferring the geostrophic and vertical velocity fields. *J. Geophys. Res.,* **101,** 16 291–16 303.

Sakamoto, T., 1999: On discontinuities in the Sverdrup interior. *J. Phys. Oceanogr.,* **29,** 2457–2461.

Shum, C. K., R. A. Werner, D. T. Sandwell, B. H. Zhang, R. S. Nerem, and B. D. Tapley, 1990: Variations of global mesoscale eddy kinetic energy observed from Geostat. *J. Geophys. Res.,* **95,** 17 865–17 876.

Sievers, H. A., and W. D. Nowlin, 1984: The stratification and water masses at Drake Passage. *J. Geophys. Res.,* **89,** 489–514.

Sinha, B., and K. J. Richards, 1999: Jet structure and scaling in Southern Ocean models. *J. Phys. Oceanogr.,* **29,** 1143–1155.

Spall, M. A., 1995: Frontogenesis, subduction, and cross-front exchange at upper ocean fronts. *J. Geophys. Res.,* **100,** 2543–2557.

——, 1997: Baroclinic jets in a confluent flow. *J. Phys. Oceanogr.,* **27,** 1054–1071.

Stevens, D. P., and P. D. Killworth, 1992: The distribution of kinetic energy in the Southern Ocean. A comparison between observations and an eddy resolving general circulation model. *Philos. Trans. Roy. Soc. London,* **338B,** 251–257.

——, and V. D. Ivchenko, 1997: The zonal momentum balance in an eddy resolving general-circulation model of the Southern Ocean. *Quart. J. Roy. Meteor. Soc.,* **123,** 929–951.

Strass, V. H., 1994: Mesoscale instability and upwelling. Part 2: Testing the diagnostics of vertical motion with a three-dimensional ocean front model. *J. Phys. Oceanogr.,* **24,** 1759–1767.

——, and Coauthors, 2000: Mesoscale dynamics: Shaping the environment of pelagic primary production at the Antarctic Polar Front. *Deep-Sea Res. II,* in press.

Tintoré, J., D. Gomis, S. Alonso, and G. Parrilla, 1991: Mesoscale dynamics and vertical motion in the Alborán Sea. *J. Phys. Oceanogr.,* **21,** 811–823.

Treguier, A. M., and J. C. McWilliams, 1990: Topographic influence on wind-driven stratified flow in a β-plane channel: An idealized model for the Antarctic Circumpolar Current. *J. Phys. Oceanogr.,* **20,** 321–343.

——, and R. L. Panetta, 1994: Multiple zonal jets in a quasigeostrophic model of the Antarctic Circumpolar Current. *J. Phys. Oceanogr.,* **24,** 2263–2277.

Vallis, G. K., and M. E. Maltrud, 1993: Generation of mean flows and jets on a beta plane and over topography. *J. Phys. Oceanogr.,* **23,** 1346–1362.

Viúdez, A., R. L. Haney, and J. Tintoré, 1996a: Circulation in the Alboran Sea as determined by quasi-synoptic hydrographic observations. Part II: Mesoscale ageostrophic motion diagnosed through density dynamical assimilation. *J. Phys. Oceanogr.,* **26,** 706–724.

——, J. Tintoré, and R. L. Haney, 1996b: About the nature of the generalized omega equation. *J. Atmos. Sci.,* **53,** 787–795.

——, ——, and ——, 1996c: Circulation in the Alboran Sea as determined by quasi-synoptic hydrographic observations. Part I: Three-dimensional structure of the two anticyclonic gyres. *J. Phys. Oceanogr.,* **26,** 684–705.

Wang, D. P., 1993: Model of frontogenesis: Subduction and upwelling. *J. Mar. Res.,* **51,** 497–513.

Whitworth, T., III, and W. D. Nowlin Jr., 1987: Water masses and currents of the Southern Ocean at the Greenwich meridian. *J. Geophys. Res.,* **92,** 6462–6476.

Wilkin, J. L., and R. A. Morrow, 1994: Eddy kinetic energy and momentum flux in the Southern Ocean: Comparison of a global eddy-resolving model with altimeter, drifter, and current-meter data. *J. Geophys. Res.,* **99,** 7903–7916.

Woods, J. D., R. Onken, and J. Fischer, 1986: Thermohaline intrusions created isopycnically at oceanic fronts are inclined to isopycnals. *Nature,* **322,** 440–449.